Supplementary Information

Ethylenediamine Addition Improves Performance and Suppresses Phase Instabilities in Mixed-Halide Perovskites

*Margherita Taddei,[1] Joel A. Smith,[2] Benjamin M. Gallant,[2] Suer Zhou,[2] Robert J. E. Westbrook,[1] Yangwei Shi,[1,3] Jian Wang,[1] James N. Drysdale,[2] Declan P. McCarthy,[4] Stephen Barlow,[4] Seth R. Marder,[4,5] Henry J. Snaith[2] and David S. Ginger[1]**

AUTHOR ADDRESS**:** Department of Chemistry, University of Washington, Seattle, WA, 98195, USA

AUTHOR INFORMATION

1 Department of Chemistry, University of Washington, Seattle, WA, 98195, USA

2 Department of Physics, University of Oxford, Oxford, OX1 3PU, U.K.

3 Molecular Engineering & Sciences Institute, University of Washington, Seattle, WA, 98195, USA

4 Renewable and Sustainable Energy Institute, University of Colorado Boulder, Boulder, CO, 80303, USA

5 Department of Chemical and Biological Engineering and Department of Chemistry, University of Colorado Boulder, Boulder CO, 80303, USA

* Corresponding author: dginger@uw.edu

Experimental Methods

Materials:

Films prepared at the University of Washington: Lead bromide ($PbBr_2$, 99.998% metals basis), and cesium iodide (CsI, 99.999% metal basis) were purchased from Alfa Aesar. Lead iodide (PbI_2, perovskite grade) was purchased from Tokyo Chemical Industries ltd. Formamidinium iodide (FAI, >99.99%) and methylammonium iodide (MAI, >99.99%) were purchased from Great Cell Solar. Ethylenediamine (puriss. p. a., absolute ≥99.5%), ethane-1,2-diammonium iodide ($EDAH_2I_2$), ethane-1,2-diammonium bromide ($EDAH_2Br_2$), lead acetate trihydrate (99.999% trace metals basis), dimethylformamide (DMF, anhydrous), dimethyl sulfoxide (DMSO, anhydrous), anisole (anhydrous) were all purchased from Sigma-Aldrich. Films and devices prepared at the University of Oxford: Lead (II) bromide ($PbBr_2$ for perovskite precursor), lead (II) iodide (PbI_2 99.99% trace metals basis for perovskite precursor) and Me-4PACz ([4-(3,6-dimethyl-9*H*-carbazol-9-yl)butyl]phosphonic acid) were purchased from Tokyo Chemical Industries ltd. BCP (bathocuproine, 98%) and cesium iodide (CsI, 99.9% trace metals basis) were purchased from Alfa Aesar. PCBM ([6,6]-phenyl-C_{61}-butyric acid methyl ester) was purchased from Solenne. Formamidinium iodide (FAI, 99.99%) was purchased from Dyenamo. Ethanol (anhydrous) was purchased from VWR. Remaining solvents and materials were purchased from Sigma-Aldrich.

Synthesis:

The synthesis of $FA_{0.83}Cs_{0.17}Pb(I_{1-x}Br_x)_3$ thin films was all conducted inside a N_2 filled glovebox. The $FA_{0.83}Cs_{0.17}Pb(I_{0.75}Br_{0.25})_3$ precursor solutions of 1.2M were prepared dissolving 0.75 mmol of PbI_2, 0.45 mmol of $PbBr_2$,0.204 mmol of CsI and 0.996 mmol of FAI in 0.8 mL DMF and 0.2 mL of DMSO. Solutions of 1.45M were prepared mixing 0.9 mmol of PbI_2, 0.54 mmol of $PbBr_2$, 0.25 mmol of CsI and 1.204 mmol of FAI in 0.8 mL DMF and 0.2 mL DMSO. All the solutions

were stirred overnight at 600 rpm. After stirring, the solutions were filtered with a 0.2 µm PTFE filter. Ethylenediamine (EDA) was added to the precursor solution after overnight stirring in molar percentages of 1, 10, 20, 40 (density = 0.899 g/mL). Solutions were deposited after a few hours following EDA addition. Glass substates (2.5 × 2.5 cm) were cleaned through a sequential sonication of 10 minutes in soap solution, DI water, acetone, and IPA. Cleaned glass substrates were ozone cleaned for 30 min before spin coating. The precursor solution (80 µL) was deposited on the glass substrates and spin coated for 10 s at 1000 rpm (200 rpm/s) and 35 s at 5000 rpm (800 rpm/s). Anisole (Sigma Aldrich) was used as antisolvent and dropped (330 µL) after 40 s. Anisole was filtered using a 0.45 µm PTFE filter before usage. The films were annealed at 100 °C for 45 min. Then the films were stored under N_2 in the dark. Films were encapsulated with a glass substrate (2.5 x 2.5 cm) using a 2-part epoxy resin-polymercaptan glue (Epoxy Adhesive C-POXY 30 by CECCORP) mixed in ratio 1:1. Encapsulation was performed inside the glove box. Encapsulated films were left inside the glove box overnight before characterization.

For films containing diammonium salts, $EDAH_2I_2$ and $EDAH_2Br_2$ were added to the precursor solution at 10 mol% excess, after which films were synthesized following the procedure listed above. For $MAPbI_3$ films, solutions and films were prepared following the procedure from Ref.[1]

UV-Vis:

UV-Vis absorbance spectra of the thin films were carried out on an Agilent 8453 UV-Vis Spectrometer in a range of 200-1100 nm and an integration time of 0.5 s. Tauc plots were extracted calculating the absorption coefficient α using equation:

$$\alpha = \frac{2.303 * A}{thickness} \qquad (S1)$$

Where A is the absorbance corrected for background scattering. All film thicknesses were estimated to be 500 nm for Tauc plotting.

Photoluminescence:

PL spectra were acquired using Edinburgh FLS1000 spectrometer. The excitation source is a 450 W ozone-free Xenon arc lamp and the detector a Si-PMT with spectral resolution from 200 to 980 nm. The films were characterized by using the instrument solid-state samples holder and the position was held constant through all the measured samples. The emission bandwidth was kept at 2 nm and dwell time at 0.3 s.

Photoluminescence quantum efficiency (PLQE):

PLQE results are determined using a 532 nm continuous wave laser (CrystaLaser LC) as the excitation source to illuminate the samples in an integrating sphere (Hamamatsu photonics K.K). The beam intensity was fixed equal to 60 mW/cm^2. The power density was verified using an optical beam profiler. The PLQE is calculated following the formula:

$$PLQ = \frac{I_{em,sample} - I_{em.\ blank}}{I_{exc,blank} - I_{exc,sample}} * 100 \qquad (S2)$$

Where $I_{em,sample}$ and $I_{em,blank}$ are the integrated area under the curve in the emission region (650-950 nm) of the sample and the bare glass blank, respectively. The $I_{exc,sample}$ and $I_{exc,blank}$ are the integrated area under the curve in the excitation region (450-630 nm) of the sample and the bare glass blank respectively.

Time Resolved Photoluminescence:

The TRPL spectra at 405 nm excitation were acquired using a Edinburgh FLS1000 spectrometer with EPL-405, a 405 nm picosecond pulsed diode laser. The repetition rate is controlled by an internal trigger input and was set to 1 MHz. The emission and excitation slits were controlled to have an emission signal frequency of 1 to 2% of the start rate. The slits were kept constants for all

the measurements and the film stage was moved in the x direction to maximize the emission. A PMT-900 detector was used in TCSPC mode with an instrumental response width of approximately 600 ps.

PL decay traces were fitted using a stretched-exponential decay function shown in **Equation 1** in the main text. This decay law is typically encountered in systems with a distribution of local decay rates and the β factor can give information on the distribution of site energies. When β = 1 the decay function reduces to a single exponential and heterogeneity is negligible. When β is closer to 0, this represents a larger distribution (e.g. decay rates) and therefore more significant heterogeneity.[2] Using the experimentally measured characteristic lifetime and β values, we calculate the total distribution and obtain the average lifetime, $\tau_{stretch}$, using **Equation 2**. $\Gamma(\frac{1}{\beta})$ is defined as the gamma function:

$$\boldsymbol{\Gamma} = \int_0^\infty x^{\frac{(1-\beta)}{\beta}} e^{-x} dx \qquad (S3)$$

Hyperspectral microscope:

Hyperspectral measurements were performed using a Photon etc. IMA upright microscope fitted with a transmitted darkfield condenser and a 60X objective (Nikon Plan RT, NA 0.7, CC 0-1.2). The excitation was done using a mercury halide lamp (Nikon ultrahigh pressure 130 W mercury lamp) passing through a 500 nm short-pass filter and emission was collected through a 500 dichroic filter and 550 nm long-pass filter. The lamp has six levels of light intensity, and all the measurements were taken using the lowest intensity (ND32) with total incident power on the sample of 256 μW. The Hyperspectral Microscope uses a tunable Bragg filter to image a sample at specific wavelengths. The sample is imaged throughout the spectral range and these images are combined into a single "Hyper Cube", which carries spectral information at each pixel. This allows

for diffraction limited imaging, rather than being constrained by the spot size of the fiber optic cable. Post-processing was done in the proprietary Photon etc. PHySpec Software.

X-ray Diffraction:

XRD patterns were obtained using a Bruker D8 Discover with IμS 2-D XRD System (Cu Kα radiation at 50 W). Further XRD at the University of Oxford were collected using a Panalytical X'Pert Pro operating at 40 mA and 40 kV accelerating voltage. Powder XRD patterns and structural views were calculated and rendered using VESTA.[3]

Scanning Electron Microscopy:

SEM images were obtained using a ThermoFisher Phenom ProX Desktop SEM with an integrated energy-dispersive X-ray diffraction (EDS) detector. Acceleration voltage of the electron beam was set to 15kV for EDS elemental analysis.

ToF-SIMS:

ToF-SIMS spectra were acquired on a IONTOF TOF.SIMS5 spectrometer using a 25 keV Bi^{3+} cluster ion source in the pulsed mode. Spectra were acquired for both positive and negative secondary ions over a mass range of m/z = 0 to 800. The ion source was operated with at a current of 0.09 pA and spectra were acquired using an analysis area of 200 μm x 200 μm using 256 x 256 pixels.

Device preparation:

Me-4PACz solution was prepared based on the procedure of Ref.[4]. Briefly, a 1 $mgml^{-1}$ stock solution in anhydrous ethanol was sonicated for ~15 mins and stirred overnight, then filtered with a 0.45 μm PTFE filter. This stock solution was then diluted to 0.33 $mgml^{-1}$ (1 mM) before use. Nanoparticle (np-) Al_2O_3 was prepared by adding 100 μl of Al_2O_3 np solution to 15 ml of anhydrous isopropyl alcohol to give a 1:150 vol ratio solution, which was stirred overnight before

use. The perovskite solution was prepared first as a 1.4 M stock (typically 5 ml) containing (per ml) 199.8 mg FAI, 61.8 mg CsI, 403.4 mg PbI_2 and 192.7 mg $PbBr_2$ in 4:1 DMF:DMSO, which was stirred overnight. Before use, this solution was diluted in a 6:1 volume ratio with 4:1 DMF:DMSO and agitated plenty. Similarly, a 10 mol% EDA stock was prepared, containing 1.2 ml perovskite, 200 µl 4:1 DMF:DMSO and 11.2 µl EDA. The 0.5-3 mol% EDA additive solutions were then prepared using volumetric mixtures of these two stock solutions, with plenty of mixing and used ~1-2 hours after the EDA was added. PCBM solution was 20 mg ml^{-1} in a 3:1 chlorobenzene:dichlorobenzene mixture, mixed plenty and then filtered with 0.45 µm PTFE filter before use. BCP solution (0.5 mg ml^{-1}) in IPA was stirred overnight and heated to 70 °C if required and filtered before use.

Pre-patterned indium tin oxide substrates were cleaned by scrubbing with 1% Decon90 solution, before sonicating sequentially in 1% Decon90, ionized water, acetone and isopropyl alcohol for for ~10 minutes each, with rinsing between each step. Substrates were dried under N_2 and UV ozone treated for 30 minutes directly before use and transferred to an N_2 glovebox for fabrication with constant purging. Me-4PACz SAM solution (150 µl, 0.33 $mgml^{-1}$ in ethanol) was spread over the substrate, and after 10 seconds spin coated at 3000 rpm for 30 s, before annealing at 100 °C for 10 minutes. After cooling, 70 µl of np-Al_2O_3 was dynamically spin-coated at 6000 rpm for 30 s, with ~ 1 min annealing at 100 °C. The perovskite was spin coated at 1000 rpm (200 $rpms^{-1}$ ramp) for 10 s, followed by 35 s at 5000 rpm (1000 $rpms^{-1}$ ramp), with 170 µl of the solution dynamically coated 3 seconds into the program, and 330 µl of anisole was dropped as an antisolvent 10 s before the end of the program. With increasing EDA content, the intermediate film was observed to be highly smooth. Films were transferred to the hotplate after a few seconds and annealed at 100 °C for 45 minutes. After cooling, 50 µl of PCBM was dynamically coated at 2000 rpm onto the

perovskite surface, and dried at 100 °C for 5-10 minutes. Once cool, BCP was dynamically coated at 5000 rpm and dried at 100 °C for 2 minutes. After removing to air and patterning the devices, 100 nm of Au was thermally evaporated under high vacuum at a rate of 0.1 – 1.2 $Ås^{-1}$. Devices were left overnight in N_2 before testing.

Device characterization:

Current-voltage (J–V) and maximum power point (MPP) measurements were measured using a Keithley 2400 source meter (Keithley Instruments) in ambient air with 100 $mWcm^{-2}$ AM 1.5g irradiance from a Wavelabs SINUS-220 simulator, and in the dark. The active area of each solar cell was defined using a black metal aperture mask to either 0.25 or 1.00 cm^2 within a black holder. Reverse J–V scans were measured from 1.3 V (forward bias) to beyond short-circuit (-0.1 V) and forward scans were from short-circuit to forward bias, both at a scan rate of ~0.24 Vs^{-1}. MPP tracking measurements were performed using a "gradient descent" algorithm for 30 s to obtain the steady-state power conversion efficiency. The intensity of the solar simulator is automatically calibrated and was additionally verified periodically using a KG5-filtered Si reference photodiode (Fraunhofer ISE).

NMR:

A two-channel Bruker Avance III HD Nanobay 400 MHz instrument running TOPSPIN 3 equipped with a 5 mm z-gradient broadband/fluorine observation probe was used, with the signal from residual non-deuterated DMSO solvent used to reference the spectra.

GIWAXS:

In situ grazing-incidence wide-angle X-ray scattering data was acquired at the I07 undulator beamline at Diamond Light Source. Solutions were deposited using an *in situ* blade coater contained in an N_2 environment incorporating a syringe driver, coating surface, motorised blade,

integrated hotplate and an N_2 outlet directed at the sample acting as an air knife. Prior to data acquisition, solutions were deposited onto cleaned glass substrates, and coated with a blade with a shim height of 100 um and coating speed of 9 mms^{-1}, with gas quenching applied continuously from 30 s. Monochromatic X-rays with energy 10 keV were incident on the sample at a grazing angle of 1°, with scattering collected by a Pilatus 2M (DECTRIS) hybrid photon-counting detector at a distance of 365 mm, calibrated using an LaB6 standard. 2D detector images were acquired every 0.2 s. Data reduction was performed using scripts based on the pyFAI and pygix libraries.[5]

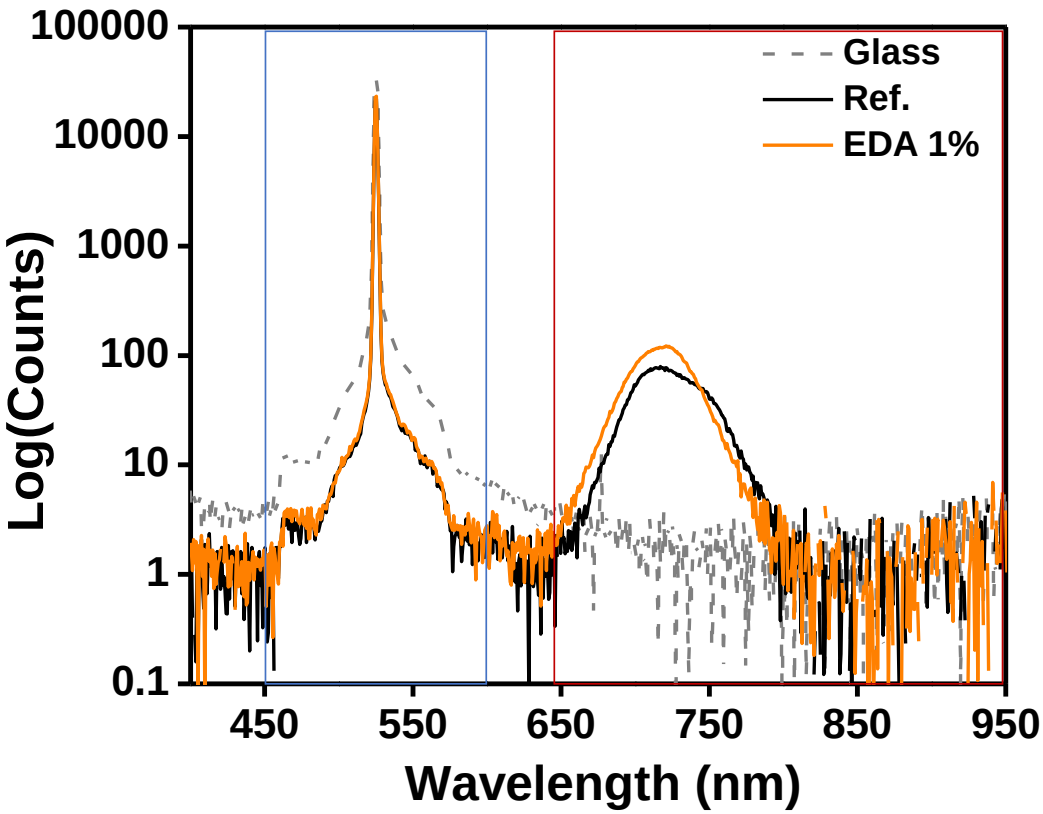

***Figure S1**: PL spectra from integrating sphere coupled with a 532 nm laser at 60 mW/cm^2. Blue lines show the excitation region and the red lines the emission region. The dashed grey spectrum is the one of a bare glass film used as blank.*

	A1	τ_c	β	$\tau_{stretch}$
EDA-0	1.21	0.58	0.17	411
EDA-1	1.05	301	0.49	627

***Table S1**: Results from the stretched exponential fitting function of photoluminescence decays shown in Figure 1b.*

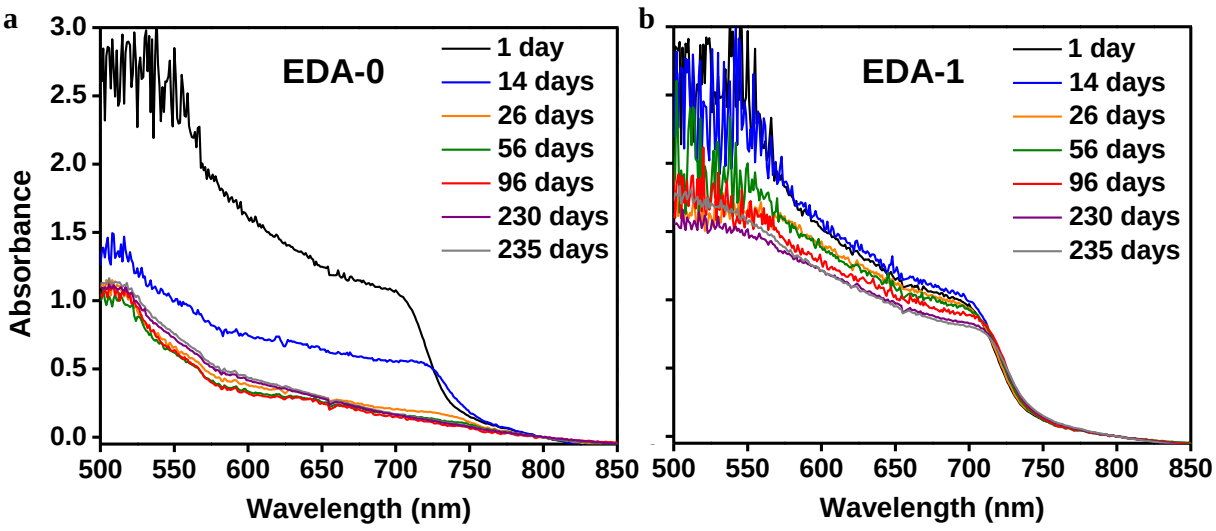

Figure S2: *UV-Vis of EDA-0, EDA-1 over 235 days of aging. The absorbance was corrected for scattering by subtracting the background signal from 850 to 1200 nm. Samples were stored unencapsulated in the dark at an average room temperature of 19.5 °C and 31% RH.*

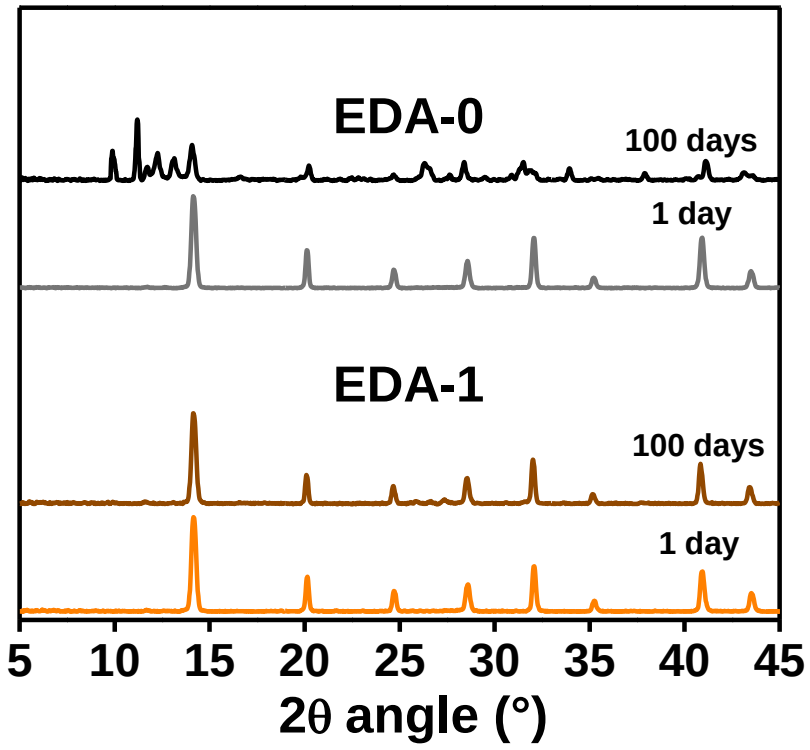

Figure S3: *XRD patterns of EDA-0 and EDA-1 after 100 days of aging. Samples were stored unencapsulated in the dark at an average room temperature of 19.5 °C and 31% RH.*

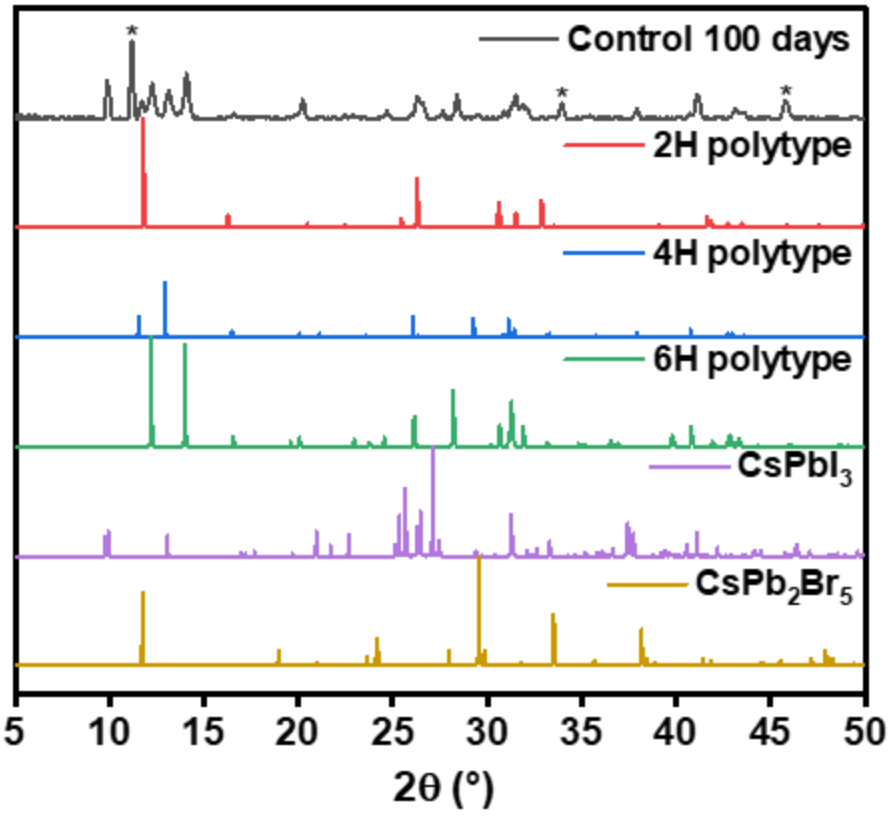

Figure S4: *XRD pattern of Control film after 100 days of aging compared against simulated powder XRD patterns for likely decomposition products 2H, 4H and 6H $FAPbX_3$ polytype phases,*[6] *$CsPbI_3$ (PDF card 01-084-2969) and $CsPb_2Br_5$.*[7] *Additional starred reflections not accounted for by these phases are consistent with a moisture-induced phase reported by Hu et al as $CsPb_2I_4Br$.*[8] *Further differences in expected peak positions may be explained by halide mixtures in the above phases.*

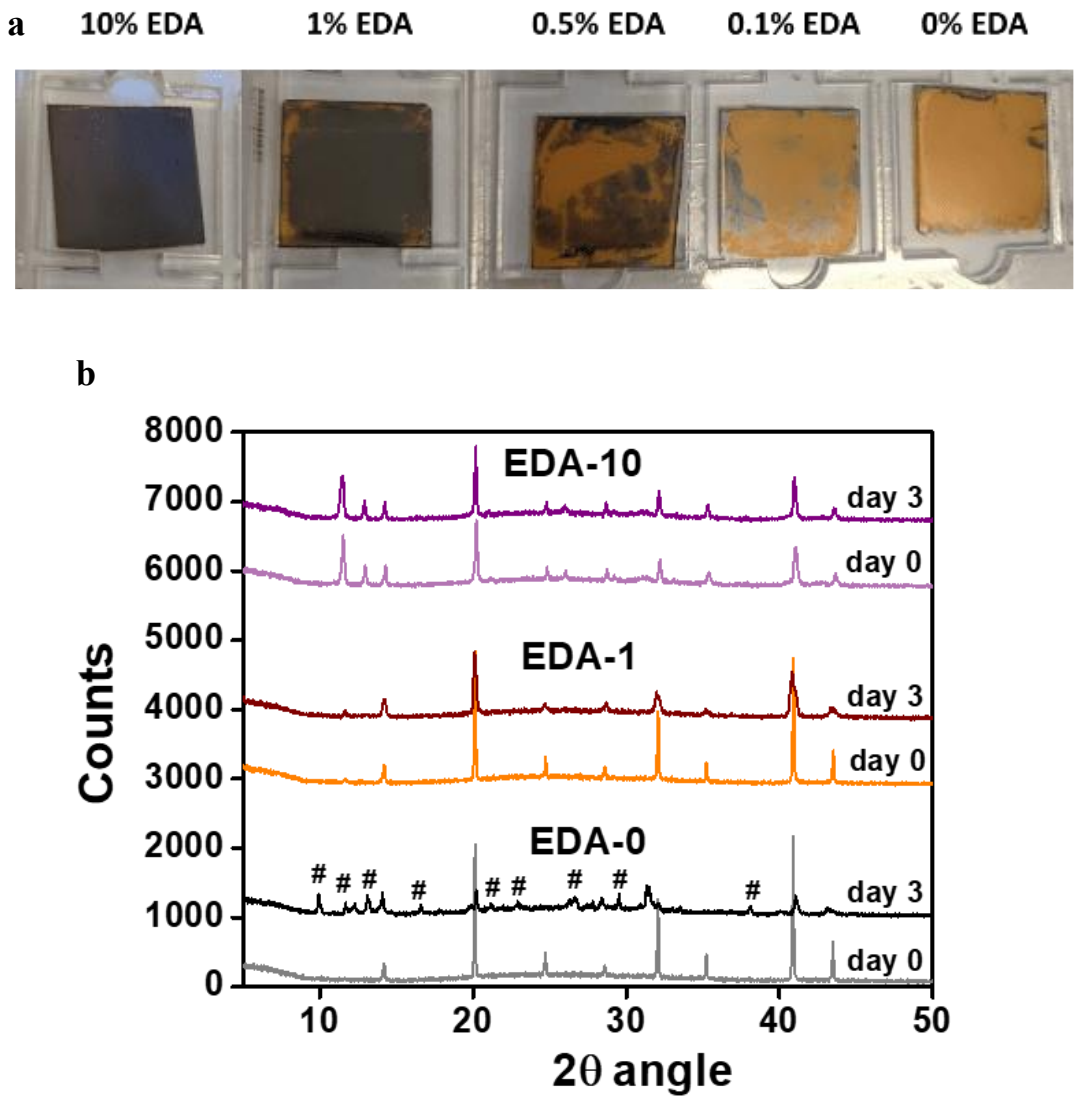

***Figure S5**: (a) Pictures of $FA_{0.83}Cs_{0.17}Pb(I_{0.75}Br_{0.25})_3$ films made at the University of Oxford after 3 days aging in ambient air, ambient room lighting, and uncovered (air flow). (b) XRD on films shown in part a. Grey, orange and pink patterns are from the films as prepared of EDA-0. EDA-1 and EDA-10. Black, dark red, and purple patterns are from the films after 3 days aging in air. Peaks marked with * are associated with 2H and 4H polytypes, please see discussion in SI Note 1. Peaks marked # denote decomposition products patterns from EDA-0 (see Fig. S4).*

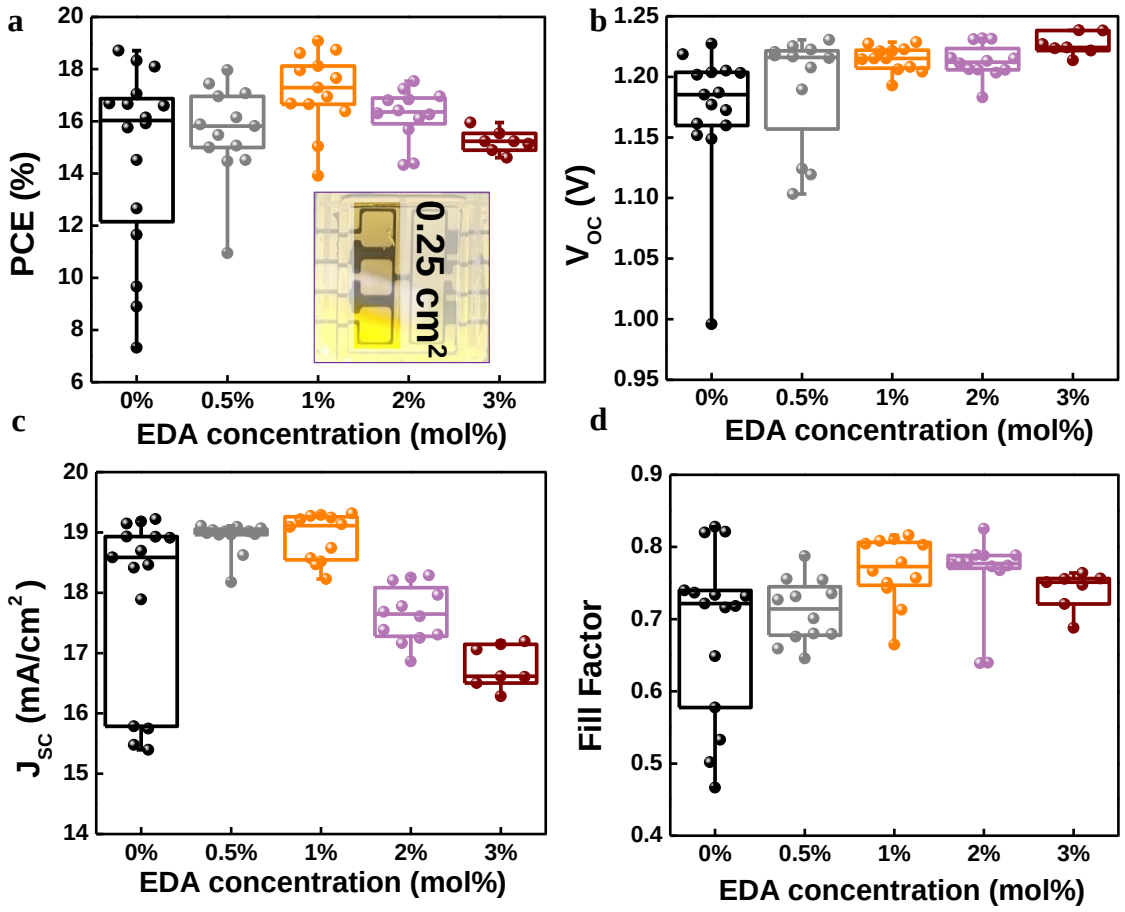

***Figure S6**: (a) Reverse sweep power conversion efficiency (PCE) (b) Open circuit voltage (V_{OC}) (c) Short circuit current (J_{SC}) and (d) fill factor (FF) of devices with 0 (black), 0.5 (grey), 1 (orange), 2 (violet) and 3 (brown) mol% of EDA in the perovskite layer. Inset: Image showing area of the device pixels.*

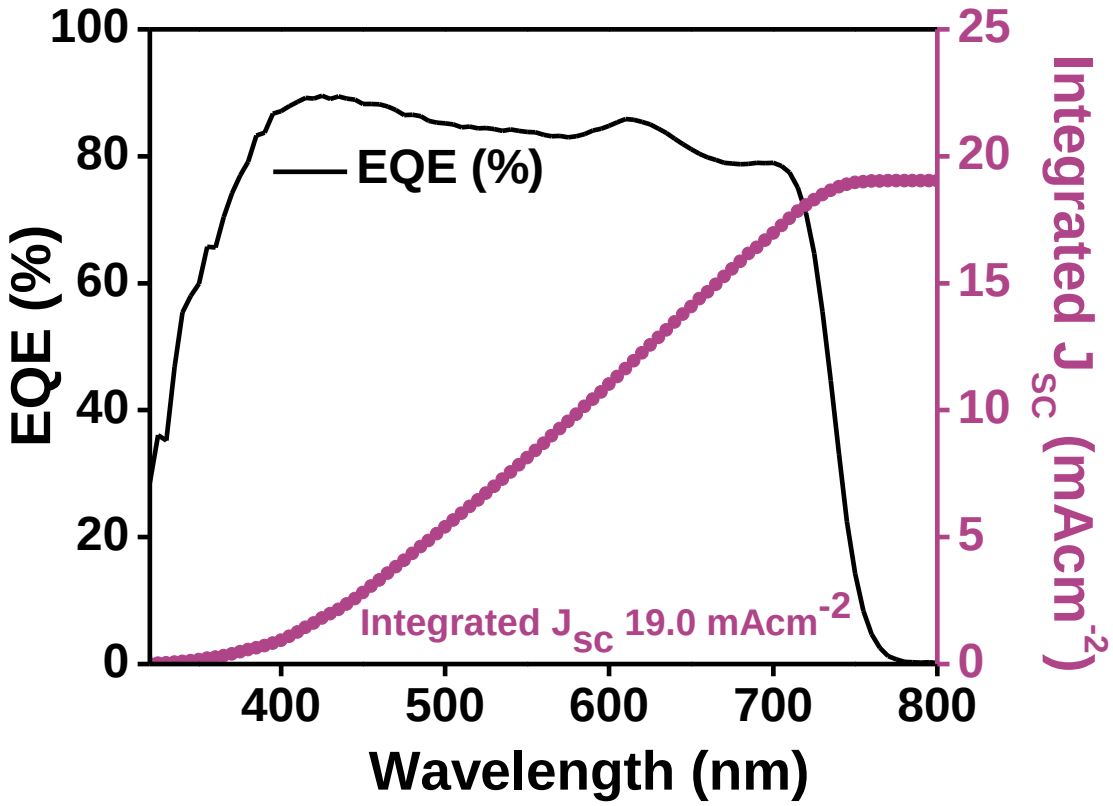

Figure S7: *Champion device (as shown in Figure 2b) external quantum efficiency (EQE) spectrum (black) and corresponding short-circuit current density (J_{SC}, purple dotted line) calculated by integration of each EQE spectrum with the global AM1.5G solar spectrum.*

DOI	Authors	Year	Bandgap (eV)	V_{OC} (V)	PCE (%)
10.1038/nenergy.2017.135	Wang et al.	2017	1.61	1.14	20.6
10.1021/acs.chemmater.8b02970	Liu et al.	2018	1.62	1.08	19.02
10.1039/c8ta04936j	Liu et al.	2018	1.625	1.12	17.65
10.1039/c5ee03874j	Saliba et al.	2016	1.63	1.058	15.4
10.1039/c8ta05795h	Svanström et al.	2018	1.64	1.02	15
10.1021/acsenergylett.8b01165	Werner et al.	2018	1.65	1.082	15.2
10.1126/science.aba1631	Lin et al.	2020	1.66	1.16	17.3
10.1002/adma.201801562	Long et al.	2018	1.67	1.19	17.92
10.1002/aenm.201902353	Raiford et al.	2019	1.68	1.162	18.43
10.1021/acsenergylett.8b01165	Werner et al.	2018	1.69	1.107	14.8
10.1021/acsami.9b17241	Bett et al.	2019	1.7	1.166	14.6
10.1016/j.mtener.2017.10.001	Yang et al.	2017	1.715	1.085	14.9
10.1002/aenm.201701048	Zhou et al.	2017	1.72	1.24	18.13
10.1021/acsenergylett.8b02179	Jaysankar et al.	2018	1.72	1.22	13.8
10.1016/j.joule.2019.05.009	Palmstrom et al.	2019	1.7	1.2	19.2
10.1021/acsenergylett.7b01255	Bush et al.	2018	1.68	1.1	15.4
our result	Taddei et al.	2022	1.685	1.22	19.07

Table S2*: List of references from which we extracted the PCE and V_{OC} values reported in Figure 3c and S8.*

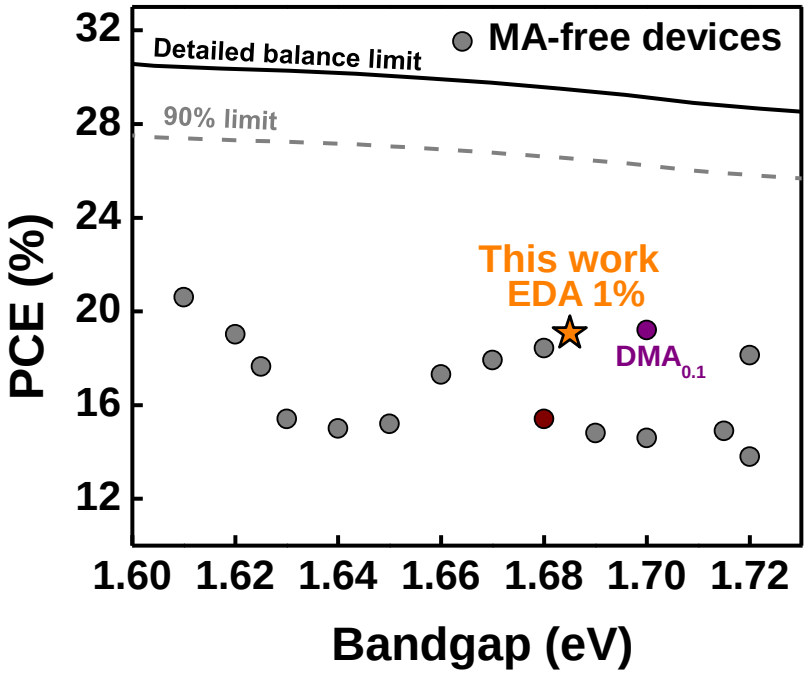

Figure S8: *Power conversion efficiencies results from the literature of wide gap devices made with* $FA_{1-y}Cs_yPb(I_{1-x}Br_x)_3$ *compositions. Purple data are from main text Ref.*[23] *using DMA+. Brown points are from Ref.*[36] *using the same perovskite composition as this work* ($FA_{0.83}Cs_{0.17}Pb(I_{0.75}Br_{0.25})_3$). *All references used are given in Table S2.*

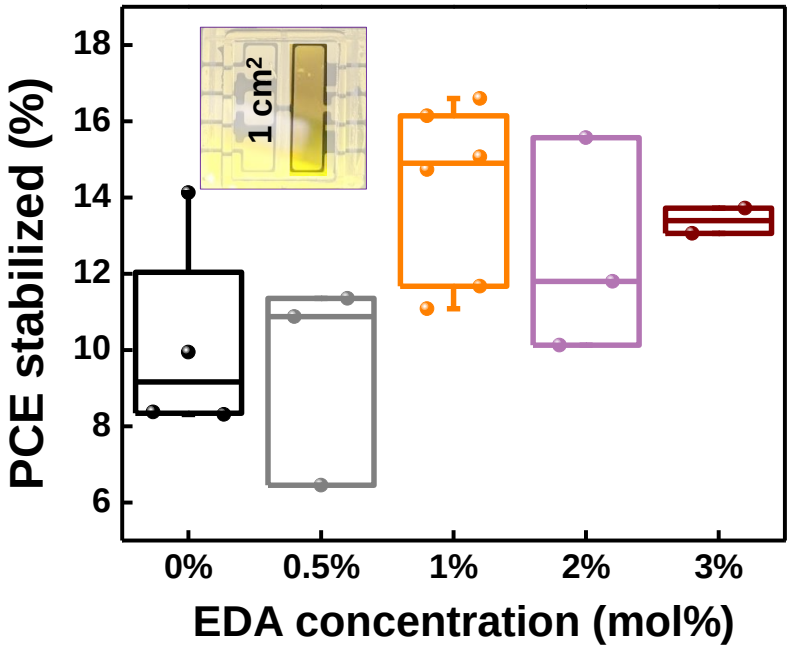

Figure S9*: Maximum power point extracted efficiency of 1* cm^2 *area devices with 0 (black), 0.1 (light grey), 0.5 (grey), 1 (orange), 2 (violet) and 3 (brown) mol% of EDA in the perovskite layer. Inset: Area of device pixel.*

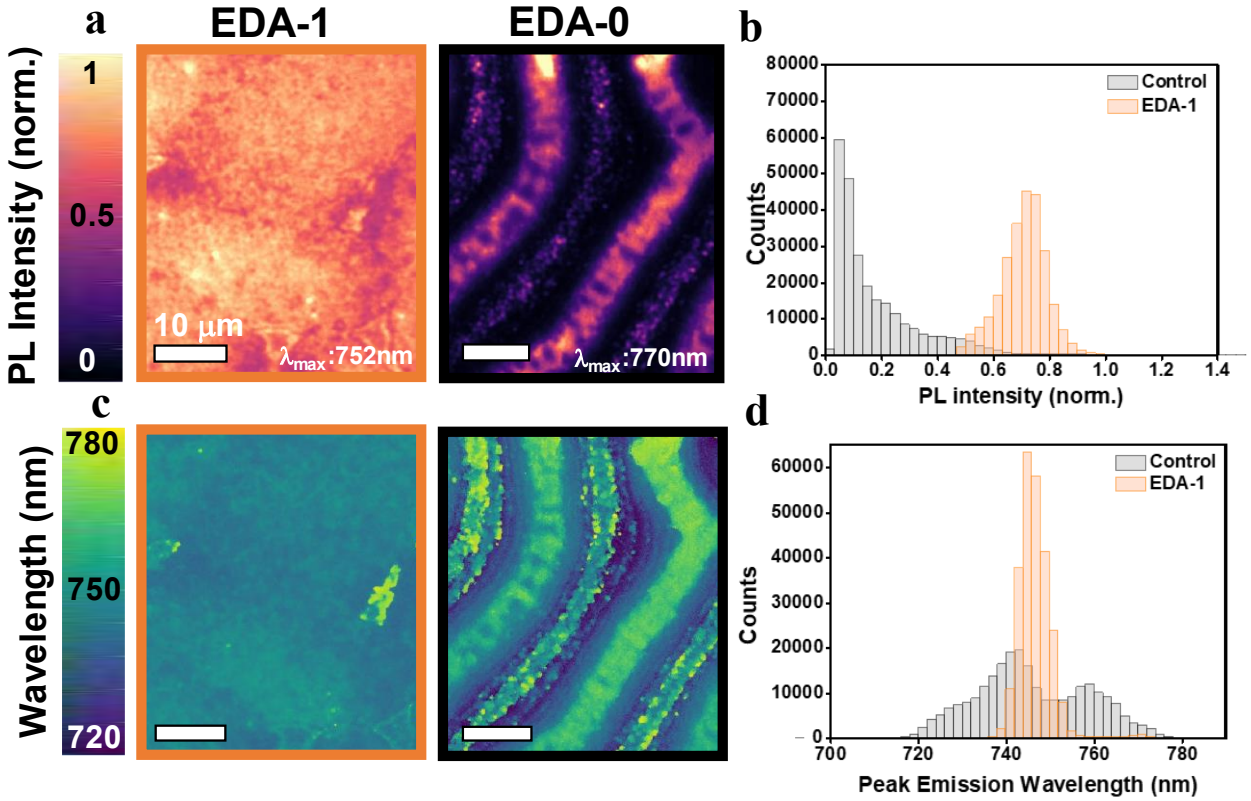

Figure S10: *(a) Hyperspectral PL intensity map of the Control film (black box) and EDA-1 (orange box). PL images are shown at the maximum emission wavelength (λ_{max}) for each sample as stated on the figure (Control λ_{max} = 772 nm, EDA-1 λ_{max} = 752 nm) (b) Histogram of the PL intensity distribution at the maximum emission wavelength for the Control (grey) and EDA-1 (orange) samples. (c) Peak emission wavelength map of the Control and EDA-1 films (d) Histogram of the distribution of peak emission wavelengths for the Control (grey) and EDA-1 (orange) samples.*

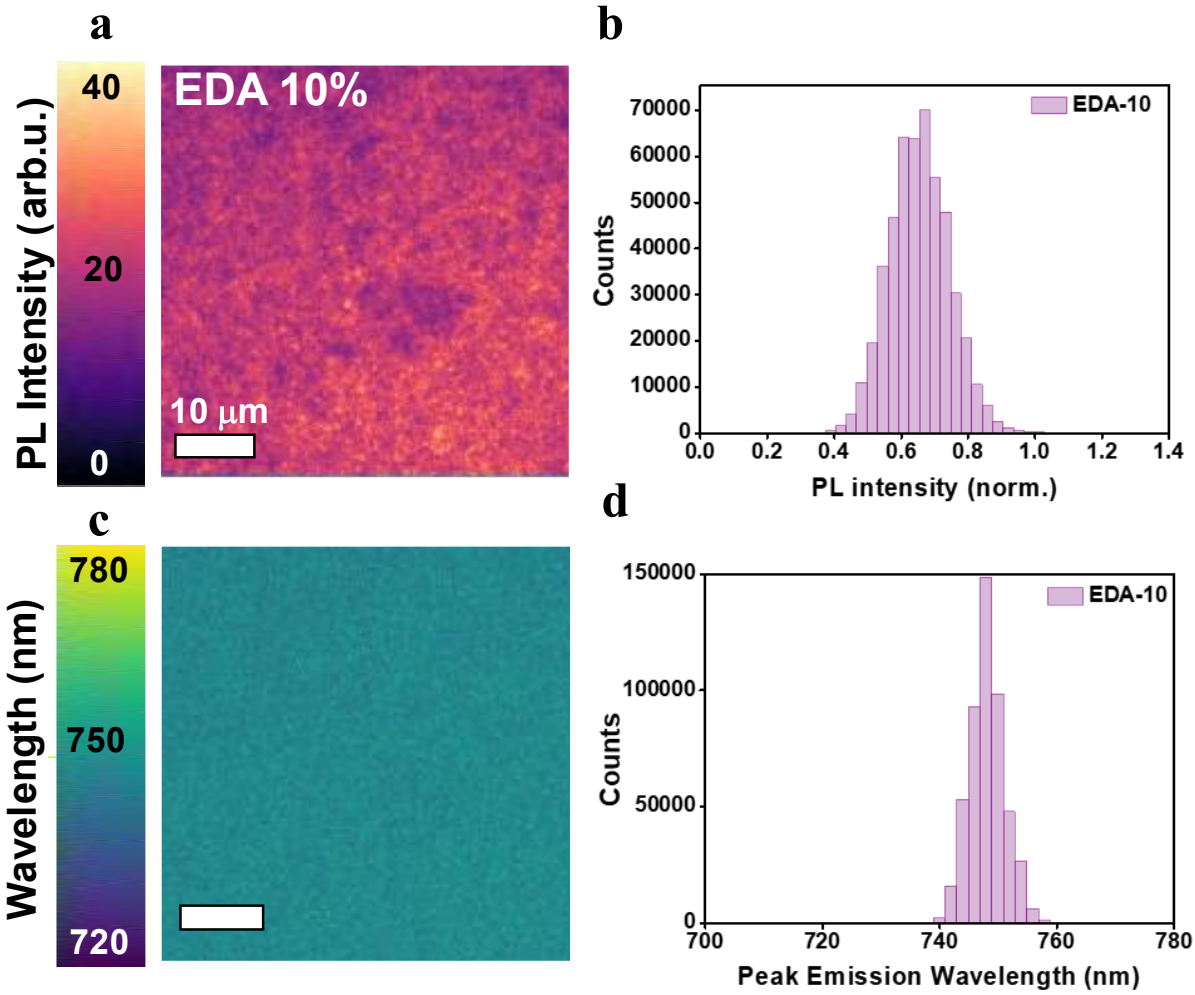

Figure S11: *(a) Hyperspectral PL intensity map of the EDA-10 sample. (b) Histogram of the PL intensity distribution at the maximum emission wavelength. (c) Peak emission wavelength map. (d) Histogram of the distribution of peak emission wavelengths.*

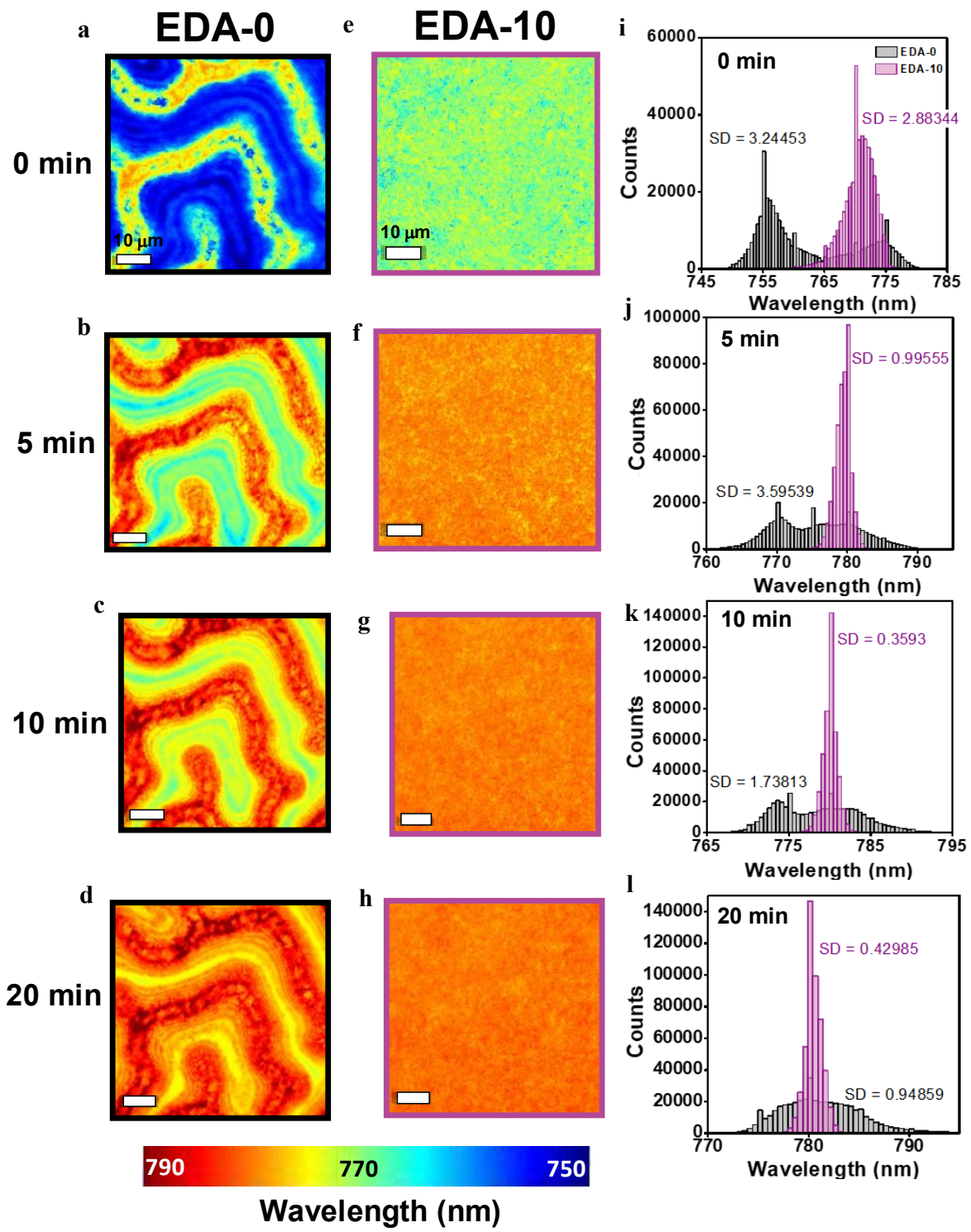

***Figure S12**: Maximum PL peak position maps extracted from hyperspectral microscopy of EDA-0 (a-d) and EDA-10 (e-h) samples. The images were taken on the same spot after soaking with a mercury halide lamp coupled to a 500 short pass filter with a power of 5 mW for 0 (a,e), 5 (b,f), 10 (c,g) and 20 (d,h) minutes. The PL peak position distribution are plotted in the histograms (i-l), of EDA-0 (grey) and EDA-10 (purple). Values of the standard deviation (SD) are indicated on the figure.*

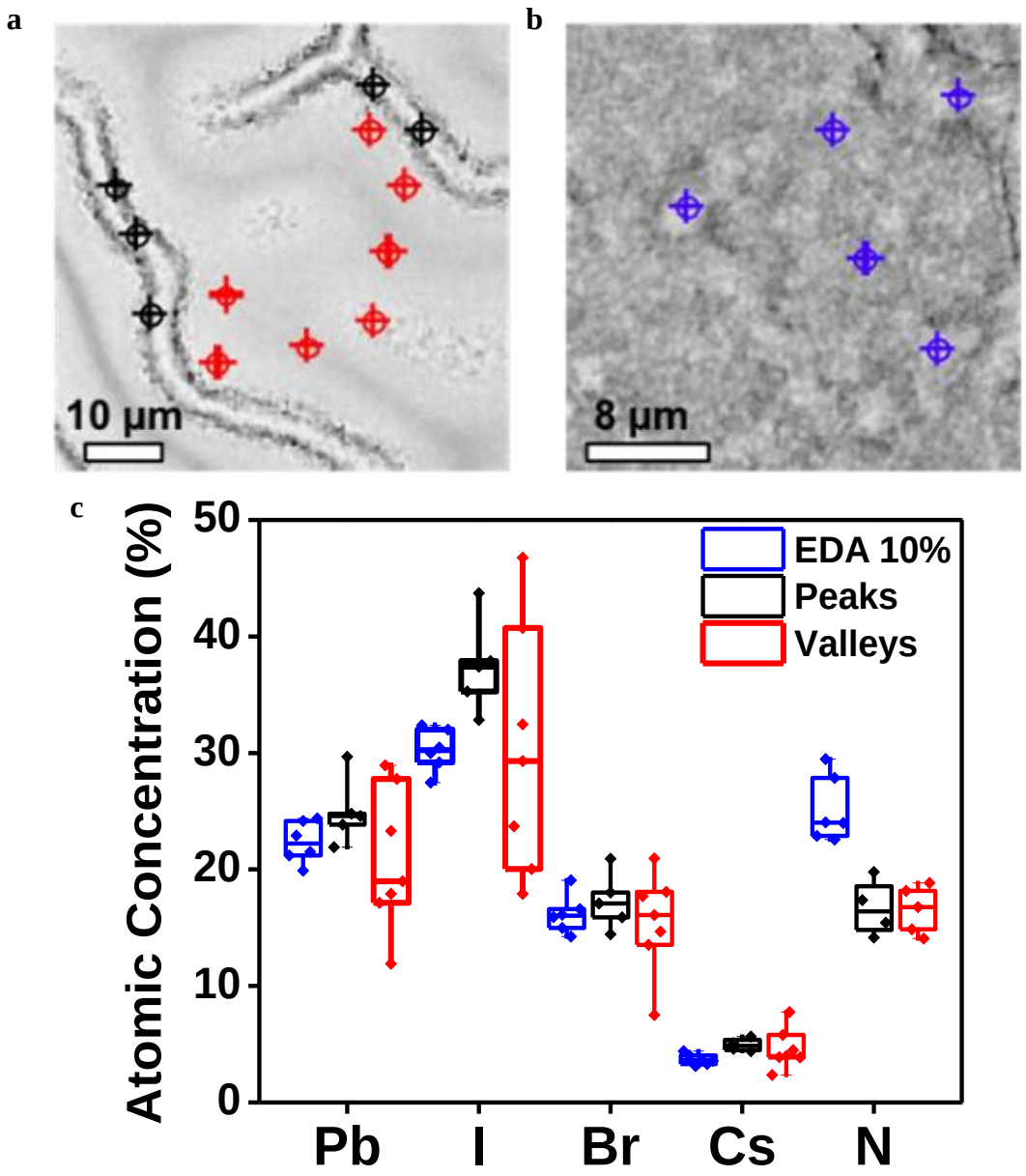

***Figure S13**: Scanning electron microscopy image of EDA-0 (a) and EDA-10 (b). The electron gun power was 15 kV from which we extracted elemental statistics by EDX shown in (c). The atomic concentration was analyzed in multiple points at the "peaks" of the wrinkles (black), in the "valleys" (red) and at several locations across the EDA-10 sample (blue).*

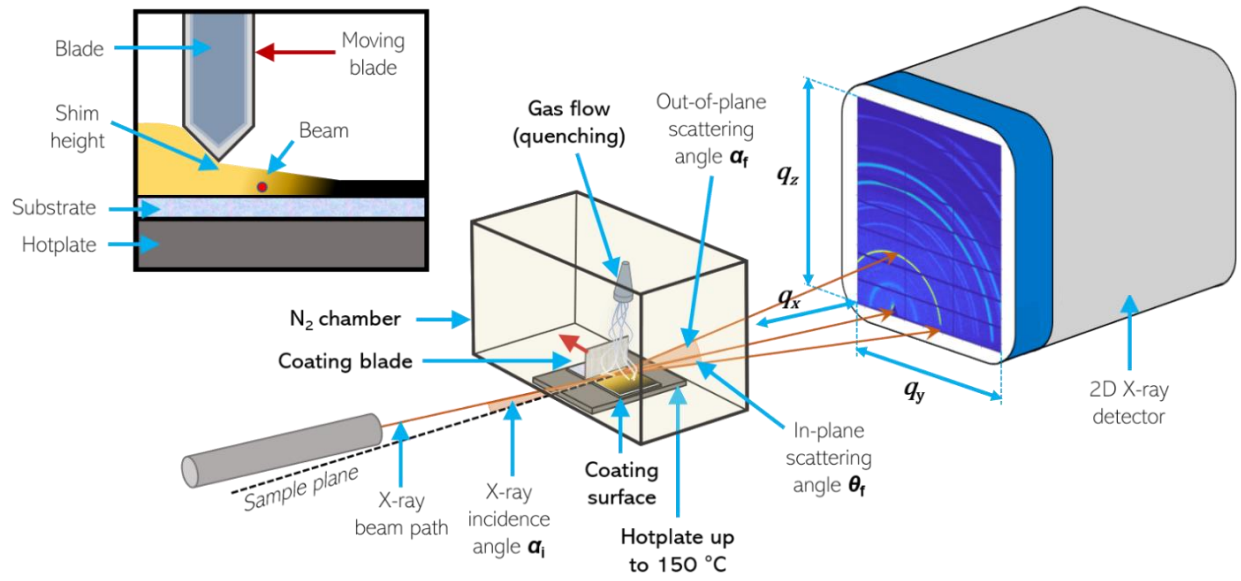

Figure S14: *Schematic illustration of GIWAXS experiments combining in-situ blade coater (moving orthogonal to the synchrotron beam), N_2 gas quenching to remove solvent and integrated hotplate for annealing. Scattering is collected with a 2D hybrid photon counting detector. Further details are given in the experimental methods.*

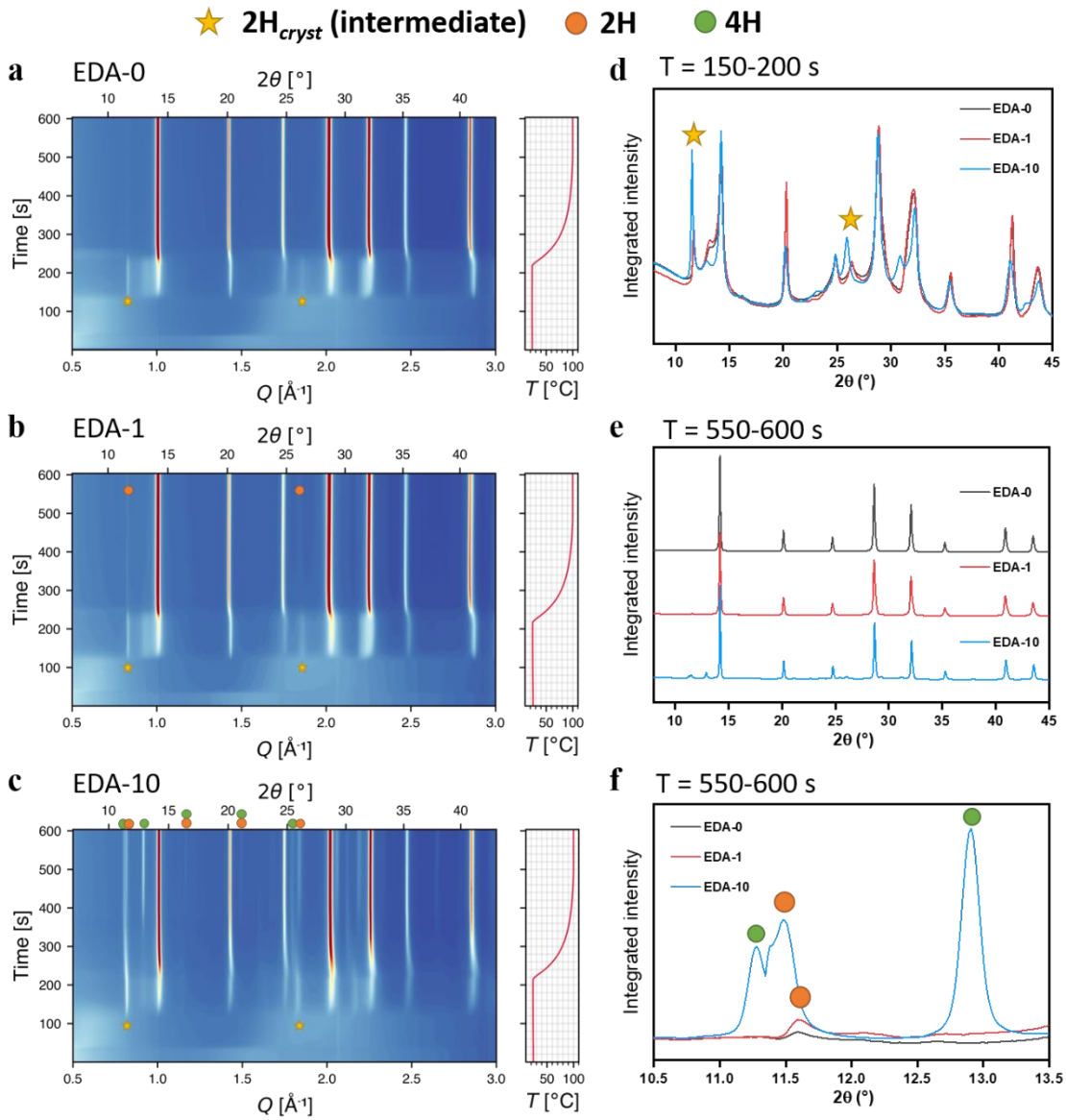

Figure S15: *In situ GIWAXS (azimuthally integrated from acquired 2D images) of blade coated solutions of (a) EDA-0, (b) EDA-1 and (c) EDA-10 samples. Peaks indicated with a yellow star indicate the characteristic reflections from a 2H polytype phase, forming as an intermediate during crystallisation, and orange and green circles indicate 2H and 4H polytype phases present after annealing. (d) Integrated 1D intensity plots from all frames between 150 and 200 s into the measurement, highlighting the initially formed 2H intermediate, which is stronger for EDA-10. (e) Integrated 1D intensity plots after heating to 100 ºC (all frames from 500-550 s), showing the dominant phase in all cases is a pseudo-cubic perovskite. (f) Highlight of part (e) showing weak scattering from a polytype at 2θ = 11.6º for the EDA-1 film, and 2H and 4H polytypes present for EDA-10.*

SI Note 1 – Phase segregation, halide sequestration and bandgap widening with EDA addition.

To understand the effect of EDA on phase behavior in thin films, we acquired XRD from films with higher additive concentrations (up to 40 mol%, EDA-40), with full patterns shown in **Figure S16**. In **Figure S17** we follow the position of the (100) reflection from the α and polytype phases. The α-phase shifts to larger 2θ angles (smaller lattice parameter) from EDA-0 to EDA-40, commensurate with the 2H/4H polytype mixture tending towards entirely 2H (reduced corner-sharing). In **Figure S18** and **S19** we show both the perovskite band-edge and the PL progressively increase in energy as the EDA concentration is increased over the same range. These changes in the XRD, PL and absorbance are all consistent with formation of an iodide-rich secondary phase, resulting in a bromide- and cesium-rich α-phase with wider bandgap. Specifically, at high concentrations, with enough of a proposed large cation present, this cation forces segregation of a pure-iodide 2H phase (**Figure S20**) while at lower concentrations (EDA-10) a 4H polytype is formed (most likely containing some bromide), having a less significant effect on altering the 3C perovskite phase composition.

To confirm the proposed perovskite bandgap widening mechanism, arising from the formation of a 1D imidazolinium lead iodide secondary phase and Cs- and Br-rich α-phase, we followed the same additive approach and investigated films of two Br-free FA-rich compositions, $FA_{0.95}Cs_{0.05}PbI_3$ and $FA_{0.83}Cs_{0.17}PbI_3$. As expected, Tauc plots from UV-Vis absorption measurements (**Figure S21**) showed only a very slight widening of the optical bandgap from the Control film to EDA-40, from 1.57 eV to 1.6 eV for $FA_{0.83}Cs_{0.17}PbI_3$ and 1.54 eV to 1.55 eV for $FA_{0.95}Cs_{0.05}PbI_3$. The bandgap from these for EDA0-40 are summarized in **Figure S22**. Moreover, in **Figure S23** we verified that the effect of bandgap widening with EDA is happening with different bromide ratios across the $FA_{0.83}Cs_{0.17}Pb(I_{1-x}Br_x)_3$ compositional space (with x= 0.15-0.28) after addition of 10 mol% of EDA. The bandgap trend is plotted against bromide content in **Figure S24.** Additionally, **Figures S25** and **S26** show that stability and PL homogeneity with EDA can be improved when added to compositions with less bromide.

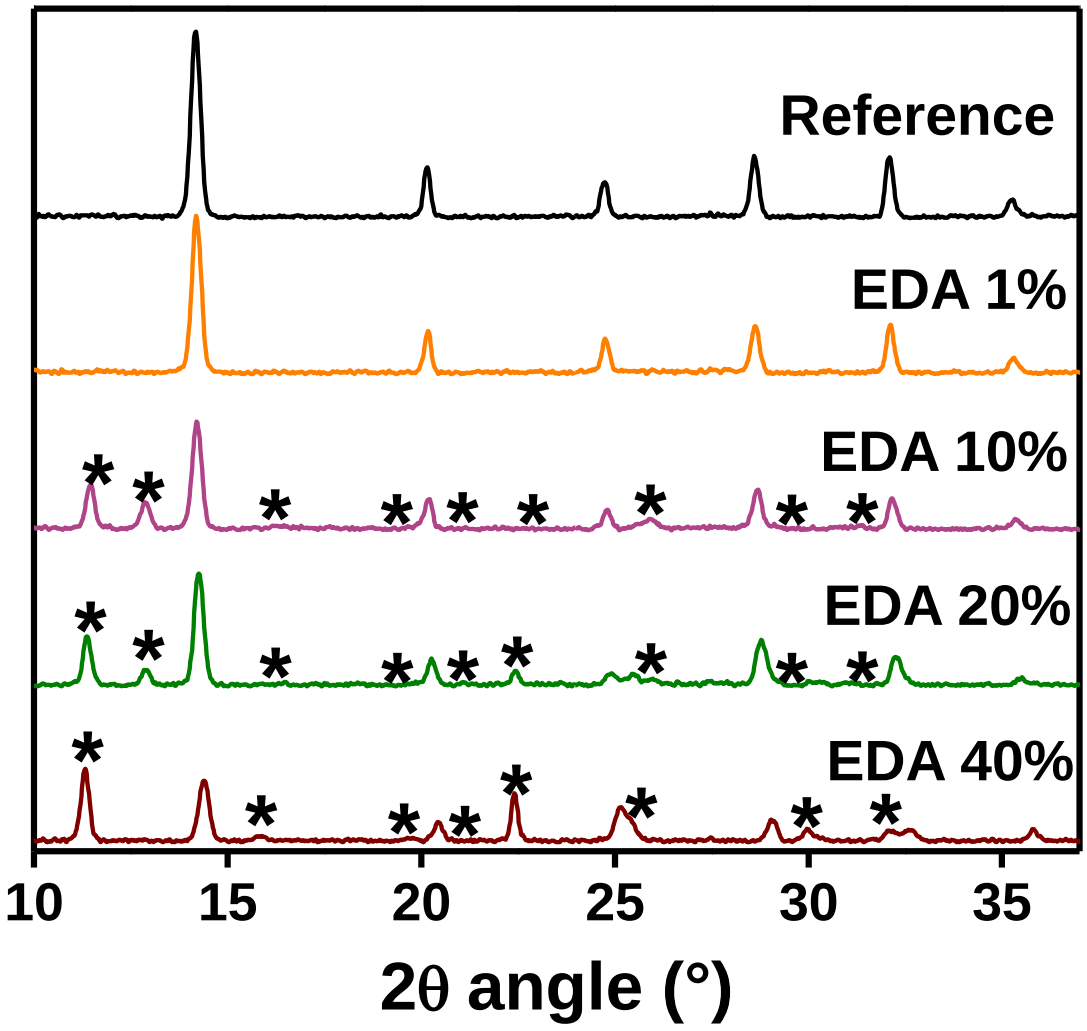

Figure S16: *XRD pattern of EDA-0 (Control, black), EDA-1 (EDA 1%, orange), EDA-10 (EDA 10%, purple), EDA-20 (EDA 20%, green), EDA-40 (EDA 40%, brown) peaks indicated with * indicates the characteristic reflections from 2H and 4H polytype phases (simulated diffraction patterns are given in Figure S4).*

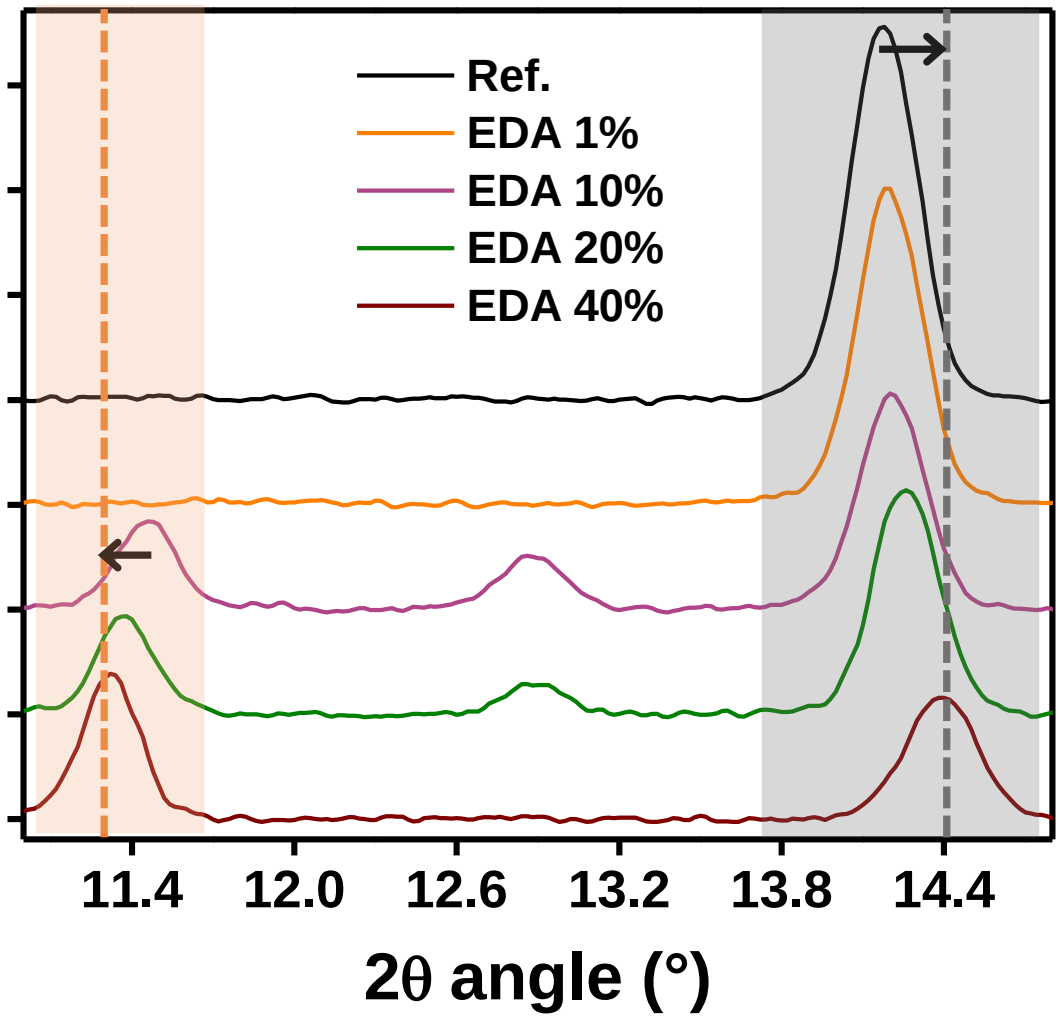

Figure S17: *Zoom on 2θ angles 11.2° to 14.6°. 2H (100) / 4H (100) peaks are highlighted in orange and cubic (100) in grey. Arrows indicate a shift of the 2H/4H (100) and cubic (100) phase with increasing EDA. Reduction of the peak at ~12.9° from the 4H polytype confirms the phase mixture in the film shifting to entirely 2H polytype at the highest EDA concentration.*

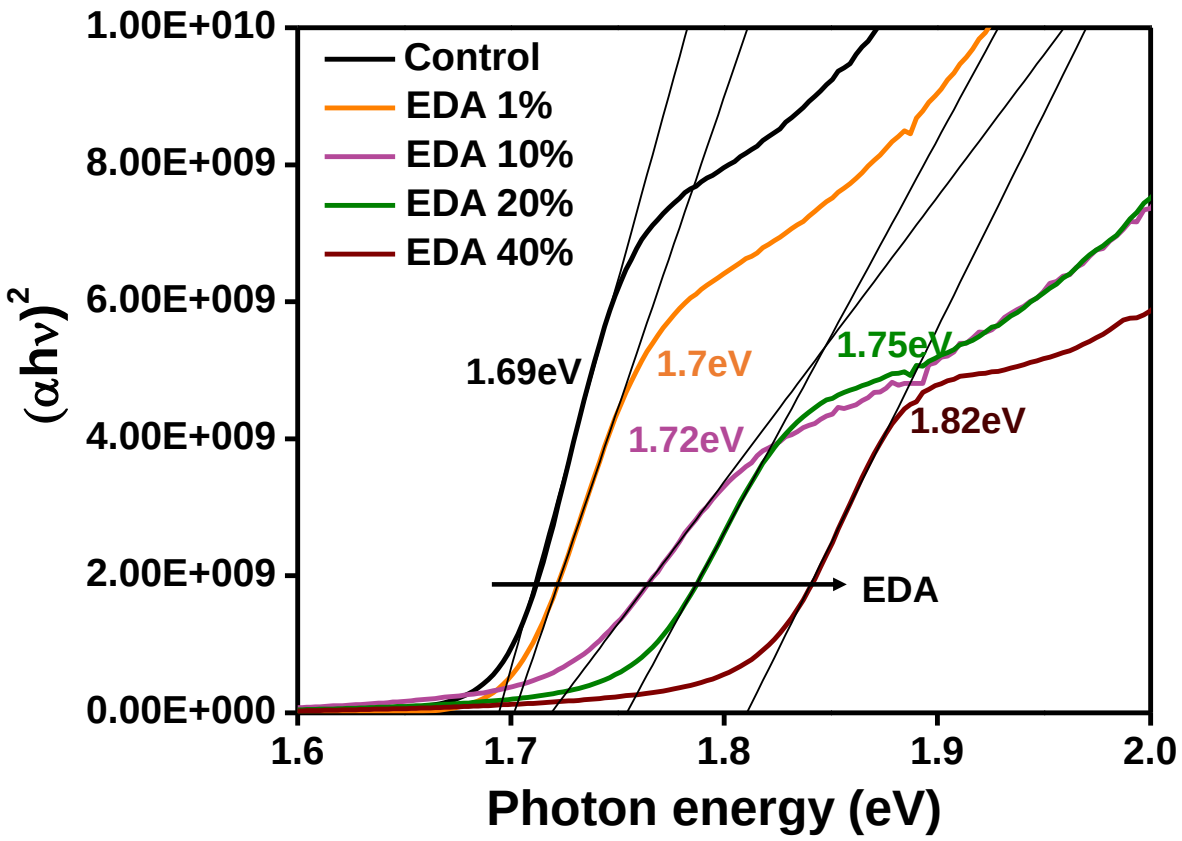

***Figure S18**: Tauc plot extracted from UV-Vis of EDA-0 (Control, black), EDA-1 (EDA 1%, orange), EDA-10 (EDA 10%, purple), EDA-20 (EDA 20%, green), EDA-40 (EDA 40%, brown). Arrows show higher E_g with more EDA added.*

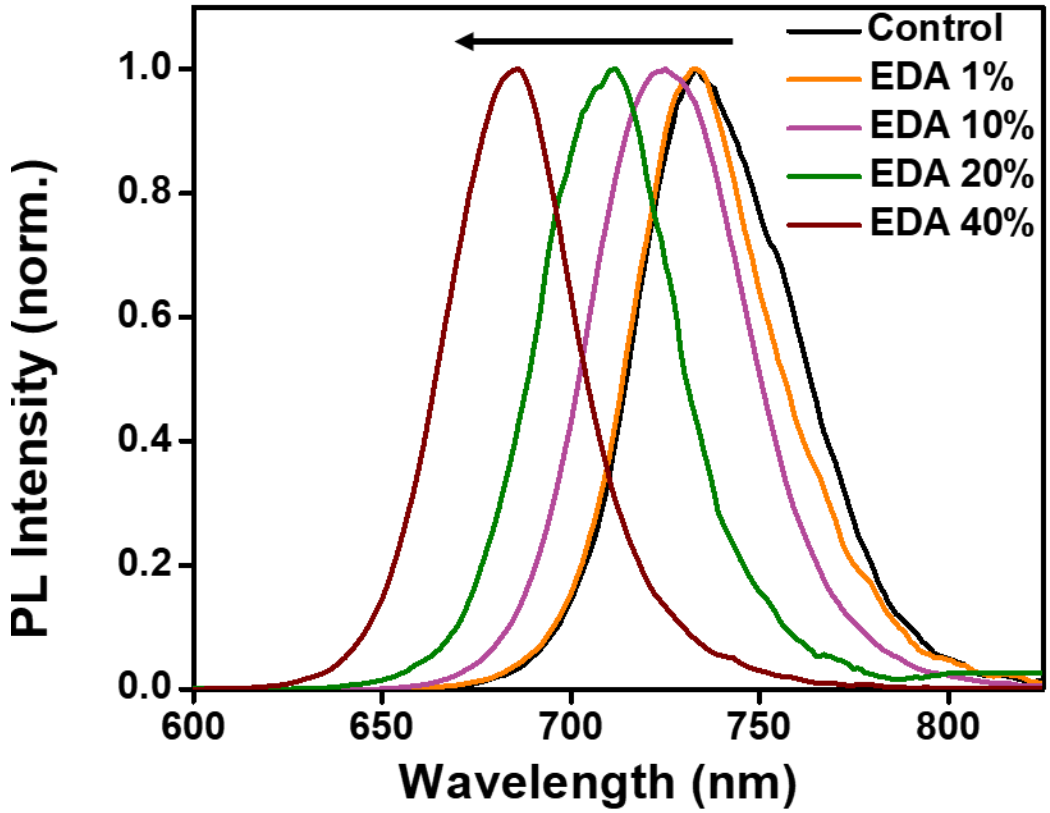

Figure S19: *Normalized steady state PL of EDA-0 (Control, black), EDA-1 (EDA 1%, orange), EDA-10 (EDA 10%, purple), EDA-20 (EDA 20%, green), EDA-40 (EDA 40%, brown) at* λ_{exc} *= 500nm.*

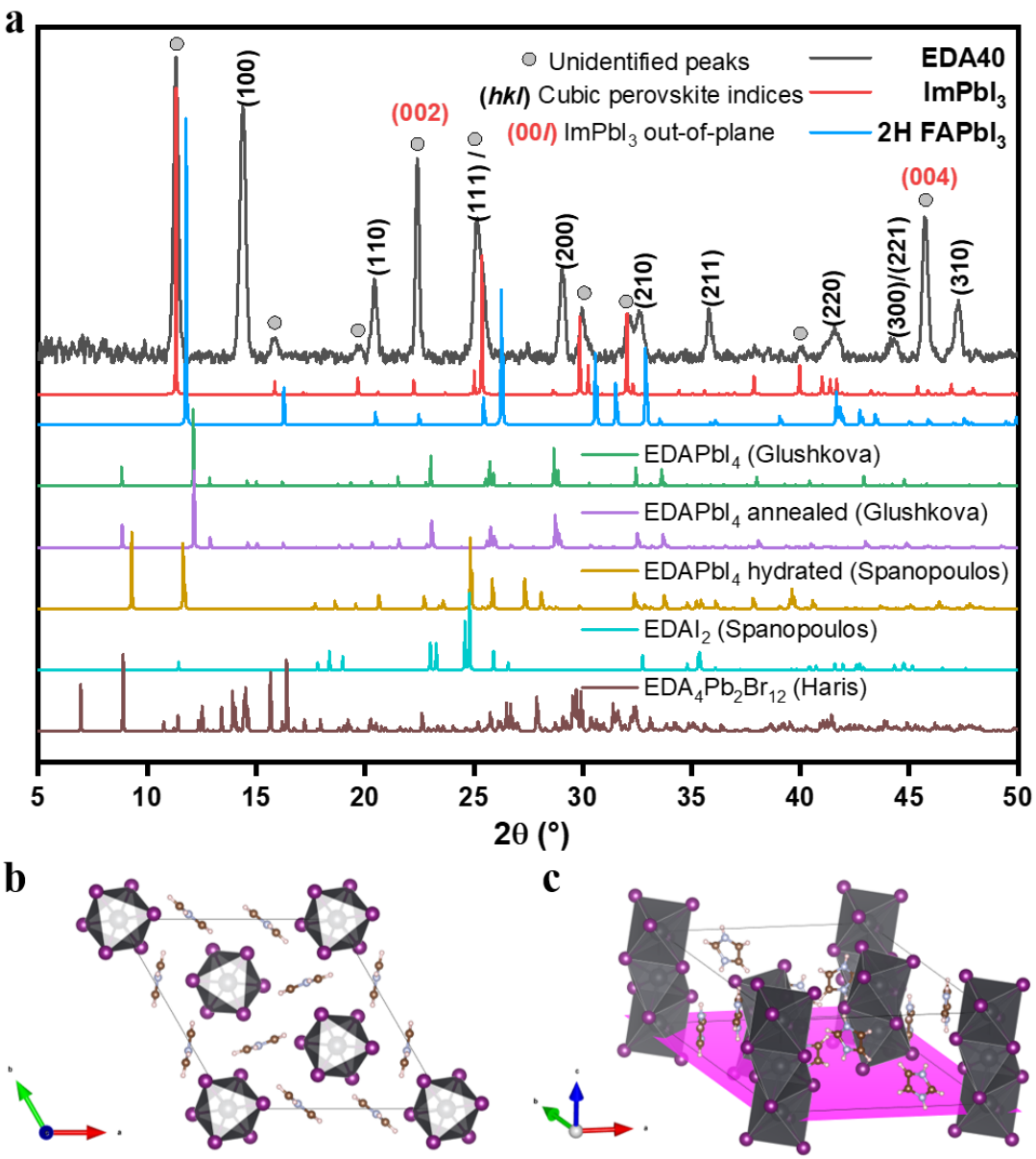

Figure S20: *(a) XRD pattern of sample with EDA 40 mol% addition (grey), simulated imidazolium lead iodide ($ImPbI_3$) 2H phase pattern (red) and $FAPbI_3$ 2H polytype (blue). Below are further simulated XRD patterns for reported $EDAPbI_4$, $EDAI_2$ and $EDA_4Pb_2Br_{12}$ phases, showing these cannot account for the additional reflections.*[9–11] *Parts (b) and (c) are projections of the $ImPbI_3$ 2H phase simulated using VESTA. In this phase the 1D iodoplumbate chains are distorted from the idealized hexagonal $P6_3/mmc$ unit cell for δ-$FAPbI_3$ due to steric effects arising from the flat imidazolium cation and are instead indexed as a larger hexagonal $P6_3/m$ unit cell. The pink plane in part c) denotes the (00l) planes which are higher intensity reflections (marked red) in the EDA-40 XRD, confirming the iodoplumbate chains are oriented in the out-of-plane direction.*

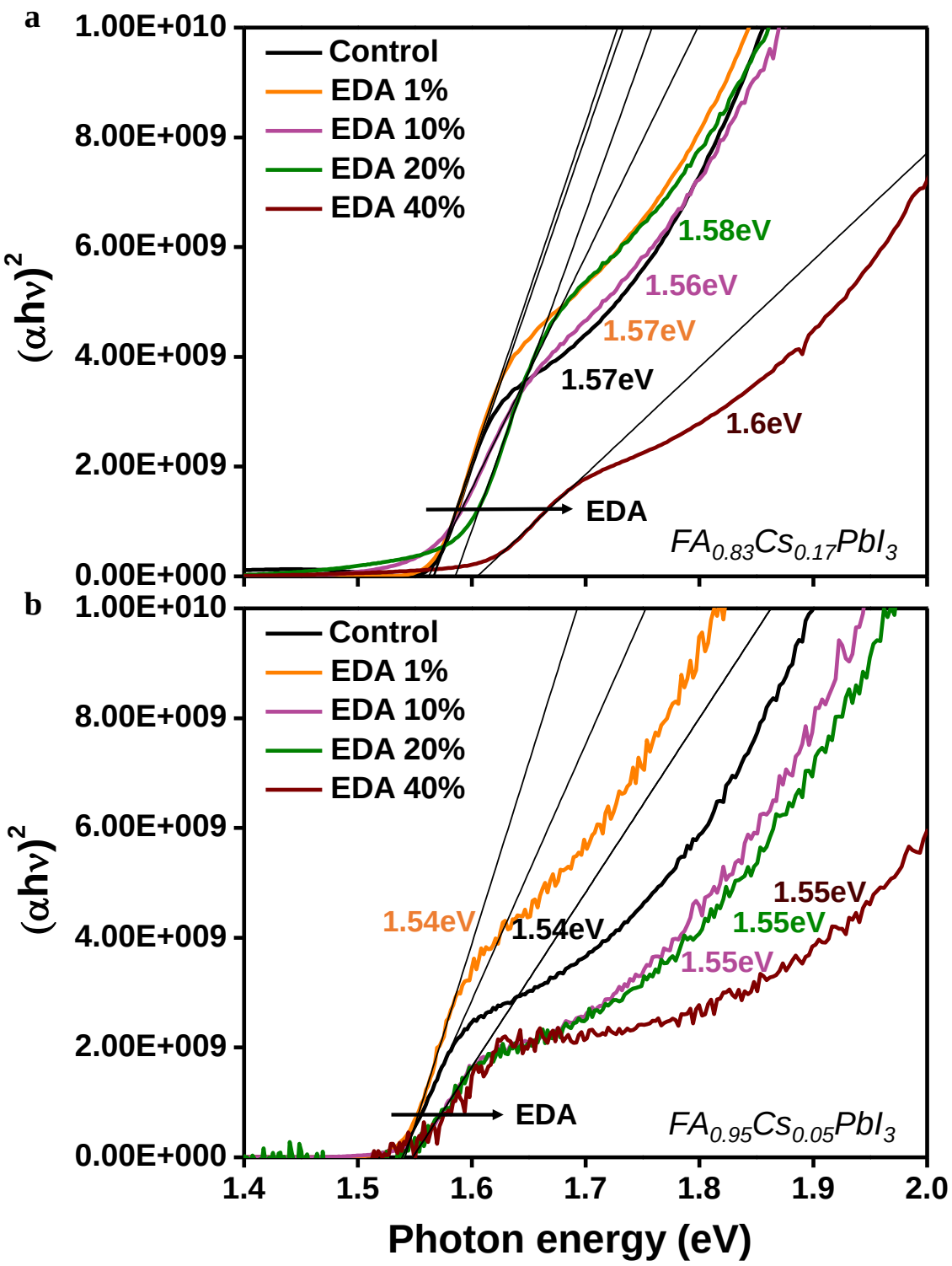

***Figure S21**: (a) Tauc plot of FA0.83Cs0.17PbI3 and (b) FA0.95Cs0.05PbI3 with EDA 0-40 mol% addition*

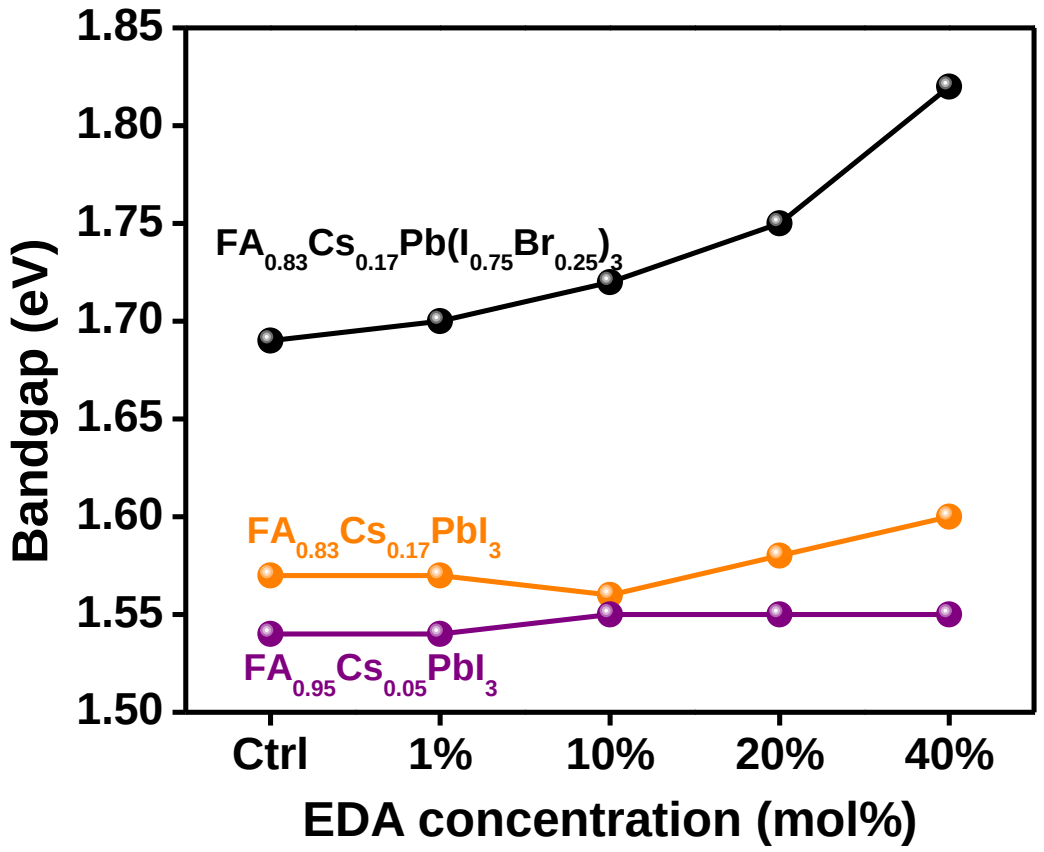

***Figure S22**: Bandgap extracted from Tauc plot shown in Figure S18 (black), Figure S21a (orange) and Figure S21b (purple) as a function of amount of EDA added in the precursor solution in mol%.*

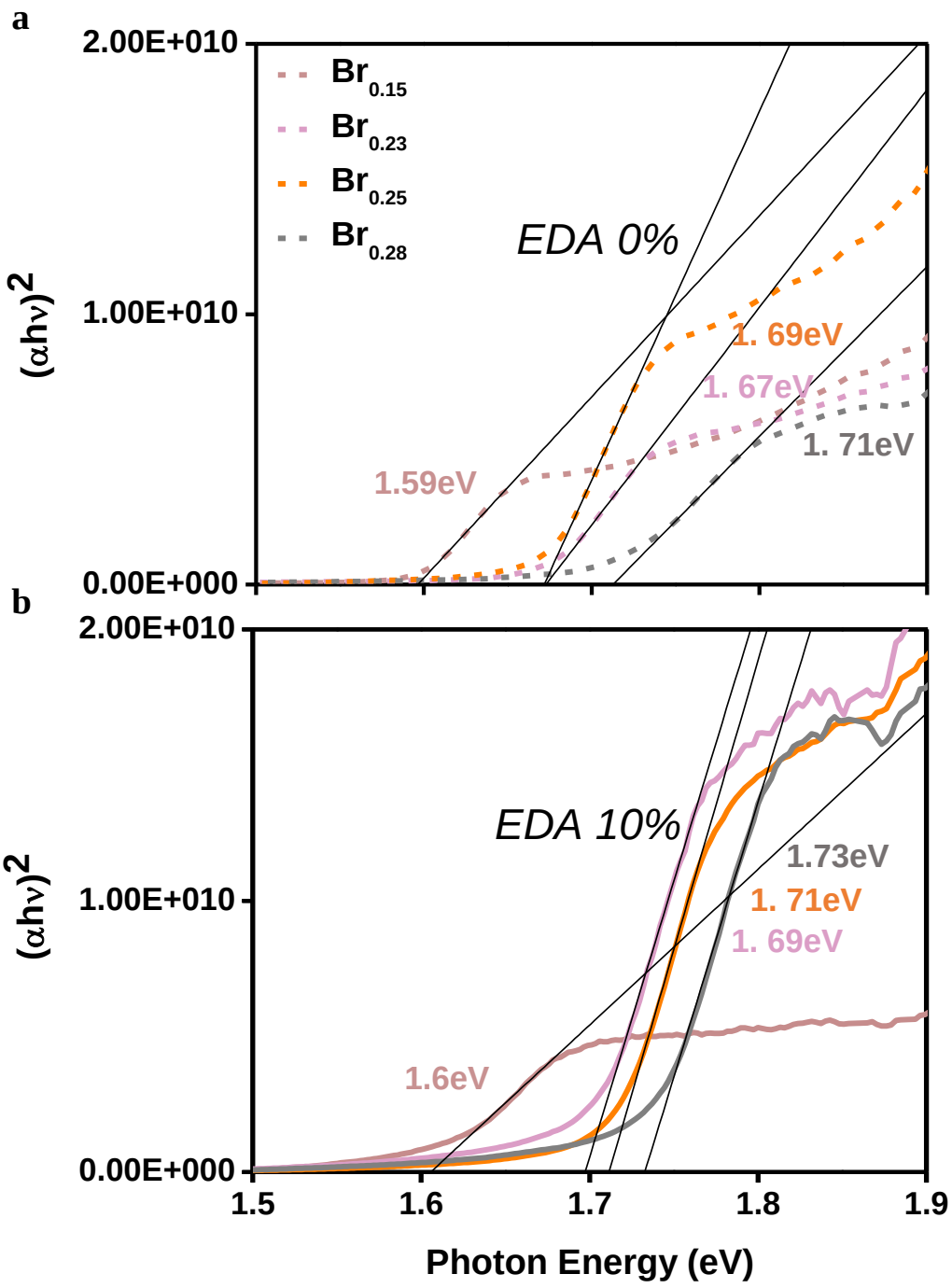

***Figure S23**: (a) Tauc plots of the EDA-0 and (b) EDA-10 $FA_{0.83}Cs_{0.17}Pb(I_{1-x}Br_x)_3$ with x=0.15 ($Br_{0.15}$, light brown), 0.23 ($Br_{0.23}$, pink), 0.25 ($Br_{0.25}$, orange), 0.28 ($Br_{0.28}$, grey).*

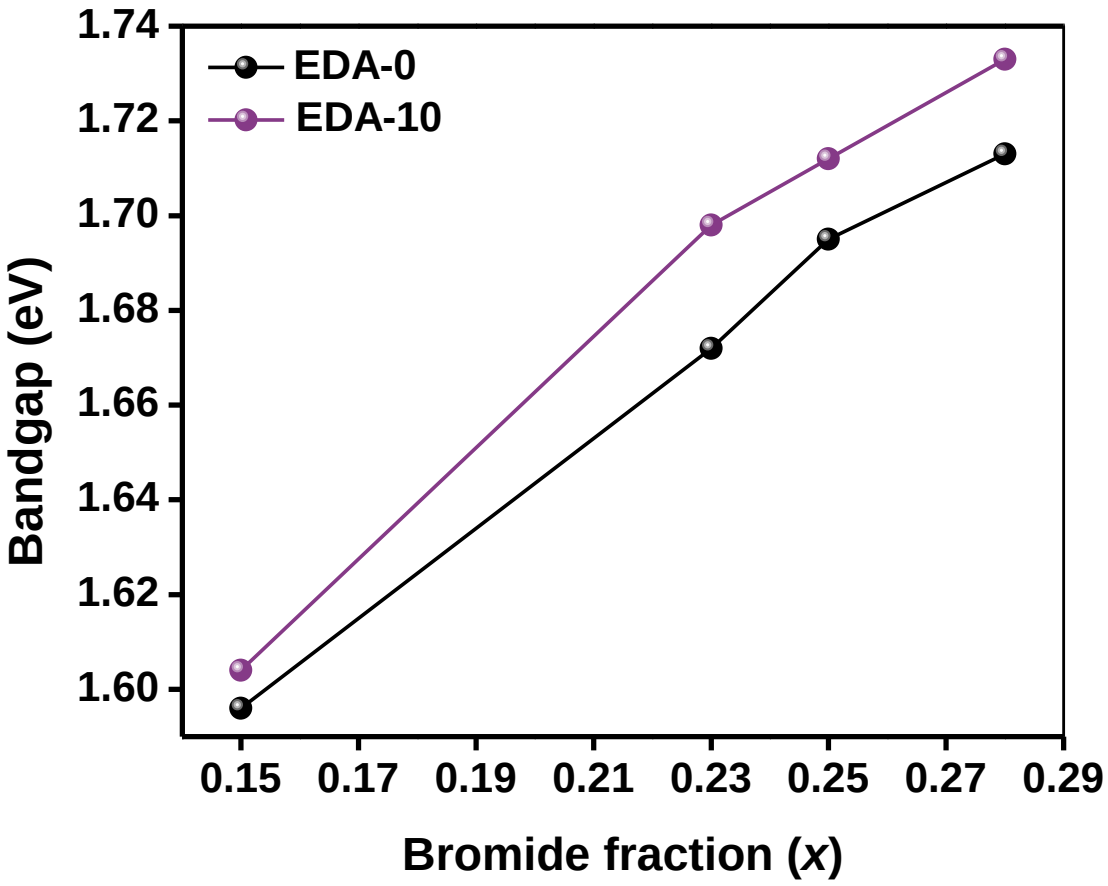

***Figure S24**: Bandgap as a function of bromide content in $FA_{0.83}Cs_{0.17}Pb(I_{1-x}Br_x)_3$ without EDA (EDA-0, black) and with EDA 10 mol% addition (EDA-10, purple) extracted from Tauc plots of Figure S23.*

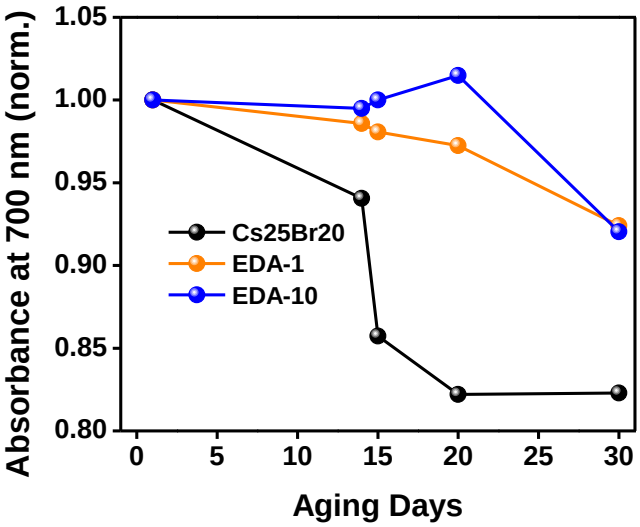

Figure S25: *Absorbance at 700 nm from UV-Vis of $FA_{0.75}Cs_{0.25}Pb(I_{0.80}Br_{0.20})_3$ (black) with addition of 1 mol% (orange) and 10 mol% (blue) of EDA over 30 days of aging recorded on day 1, 14, 15, 20 and 30 of aging. The values are normalized to day 1. Samples were stored unencapsulated in the dark at an average room temperature of 19.5 °C and 31% RH*

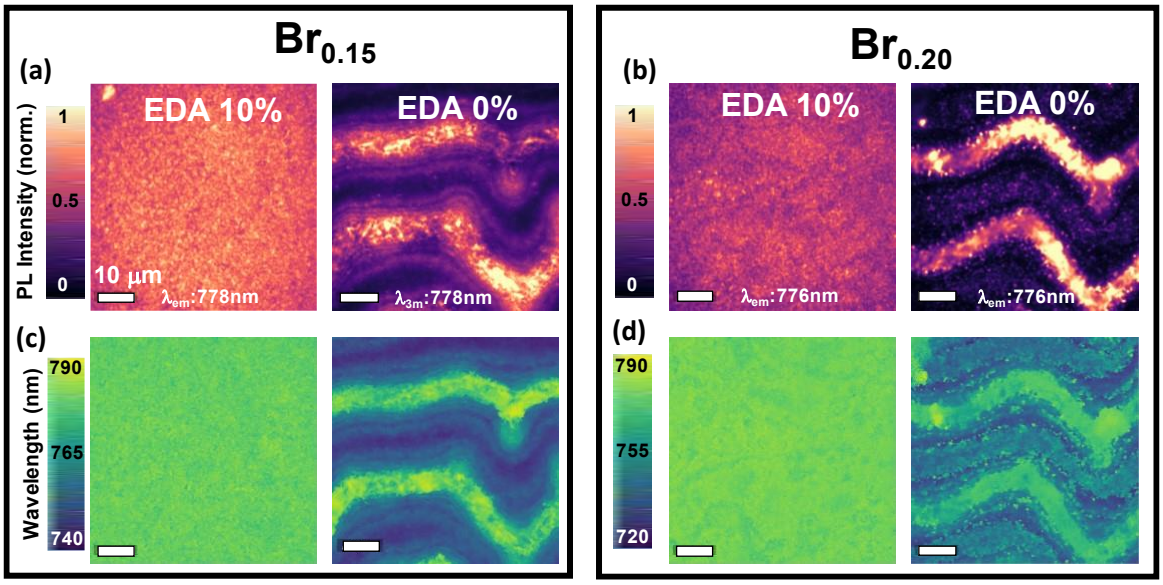

Figure S26*: (a) Hyperspectral PL intensity map of $FA_{0.83}Cs_{0.17}Pb(I_{0.85}Br_{0.15})_3$ indicated as "$Br_{0.15}$" and (b) $FA_{0.83}Cs_{0.17}Pb(I_{0.80}Br_{0.20})_3$ indicated as "$Br_{0.20}$" with (EDA 10%) and without (EDA 0%) addition EDA. PL images are shown at the emission wavelength (λ_{em}) indicated at the bottom of the figures. Excitation was achieved with a white lamp with short pass filter at 500 nm. The emission was recorded using a 500 nm dichroic and 650 nm long pass filter. (c) Peak emission wavelength map of the $Br_{0.15}$ and (d) $Br_{0.20}$ with (EDA 10%) and without (EDA 0%) addition EDA.*

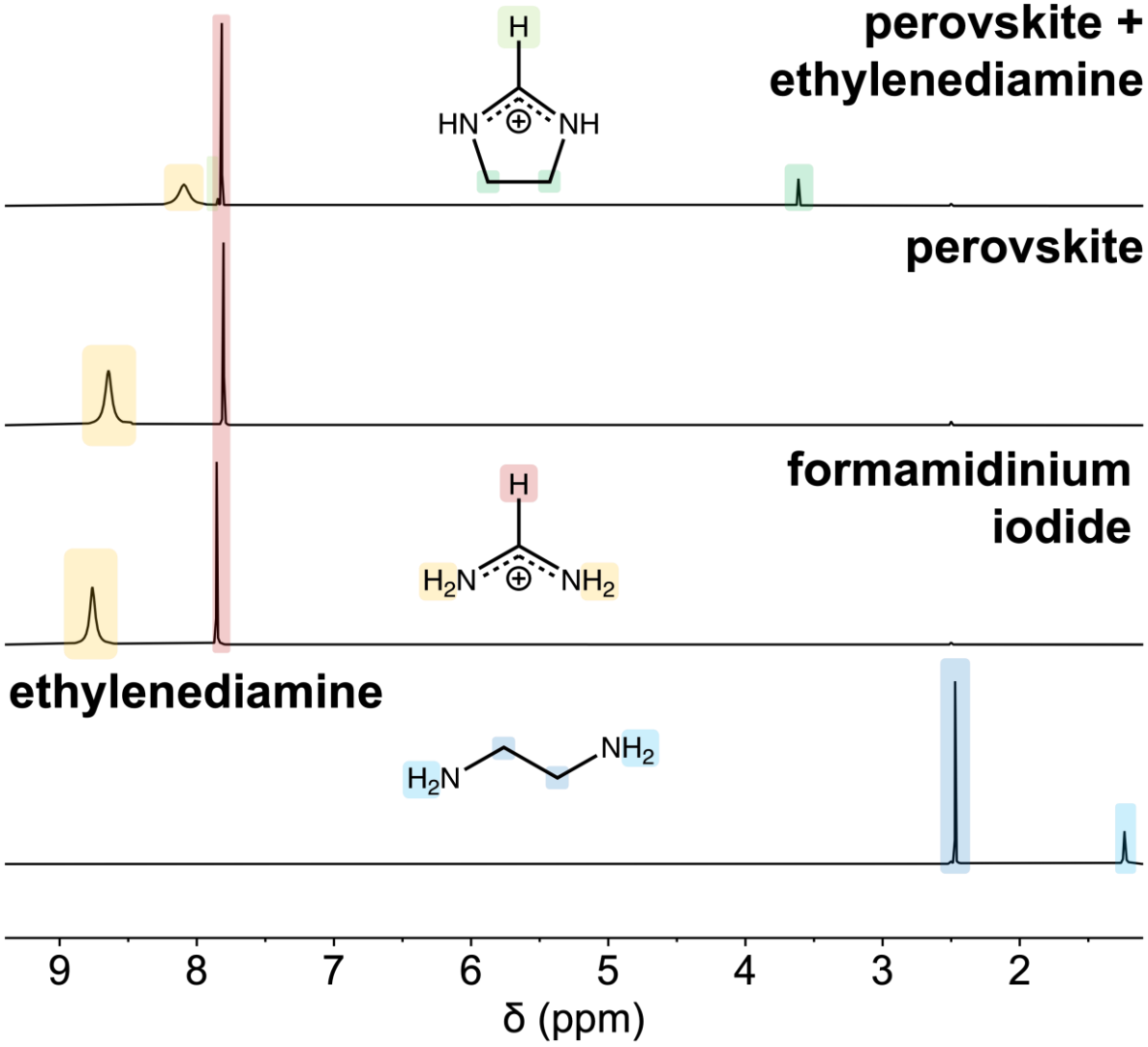

Figure S27: *Full spectra corresponding to those shown in main text* ***Figure 4a****.* ^{1}*H solution NMR spectra of (bottom to top) ethylenediamine (EDA), formamidinium iodide and* $(FA_{0.83}Cs_{0.17})Pb(I_{0.75}Br_{0.25})_3$ *without and with 10 mol% EDA added. Signals at 2.50 ppm correspond to DMSO incidentally introduced with the deuterated solvent.*

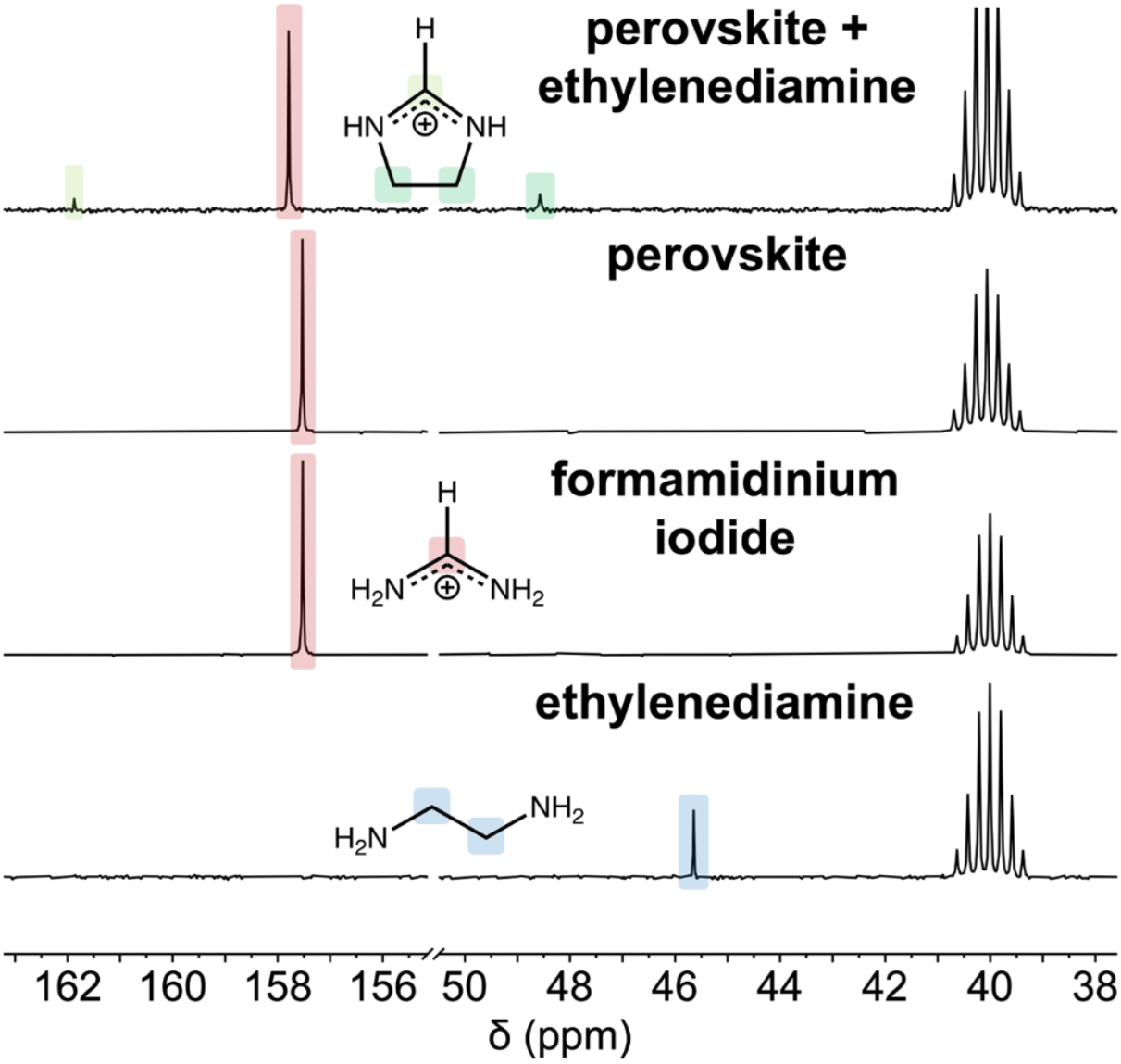

Figure S28: *^{13}C solution NMR spectra of (bottom to top) ethylenediamine (EDA), formamidinium iodide and $(FA_{0.83}Cs_{0.17})Pb(I_{0.75}Br_{0.25})_3$ without and with 10 mol% EDA added. Signals at 40.0 ppm correspond to the solvent d^6-DMSO.*

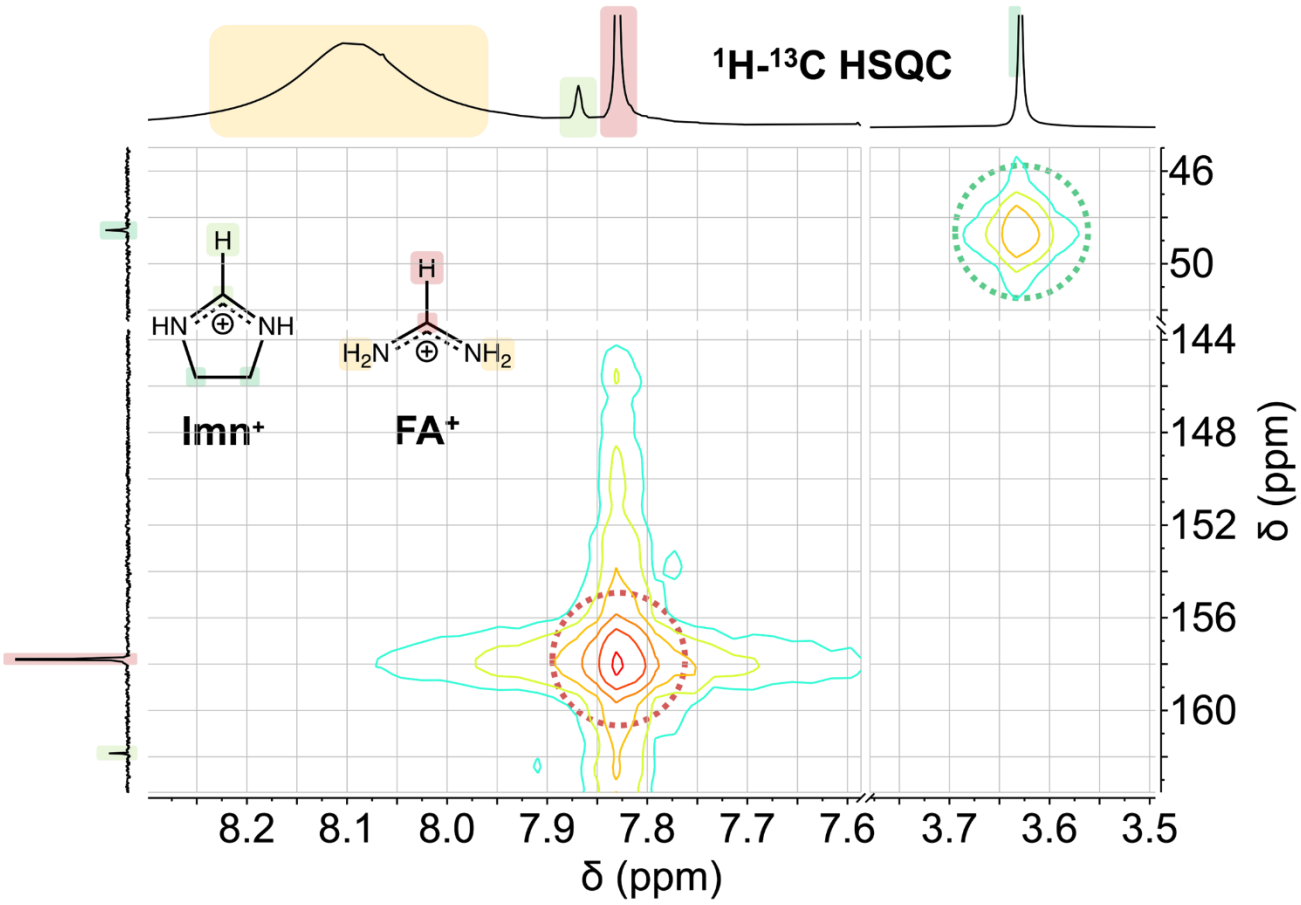

Figure S29: *^{1}H-^{13}C heteronuclear single quantum correlation spectroscopy (HSQC) of $(FA_{0.83}Cs_{0.17})Pb(I_{0.75}Br_{0.25})_3$ with 10 mol% EDA added. Signals in the 2D spectrum indicate that the corresponding proton and carbon environments are directly bonded.*

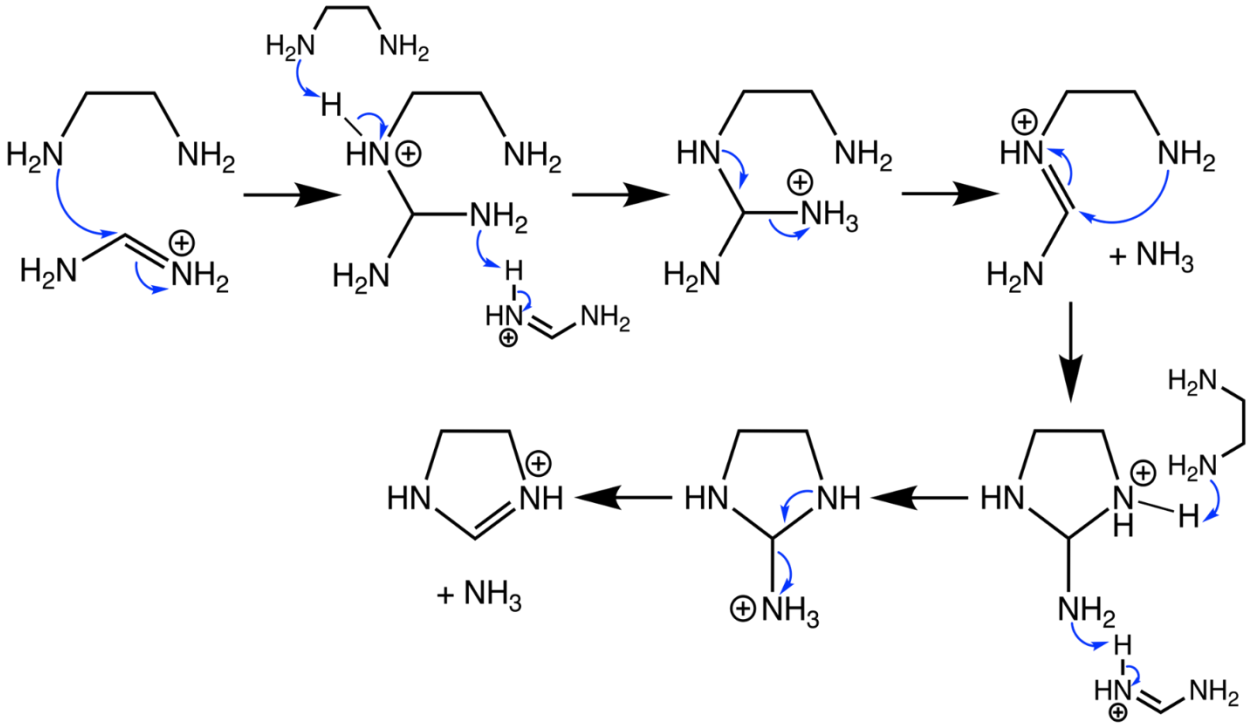

Figure S30: *Full mechanistic justification for production of 2-imidazolinium (Imn^+) from ethylenediamine (EDA) and formamidinium (FA^+). A first nucleophilic addition of EDA to FA^+ is followed by reformation of the amidinium group by elimination of NH_3, which is highly volatile and therefore likely lost from solution to the gas phase. Rapid intramolecular nucleophilic attack by the remaining amine on the reformed amidinium system leads to cyclisation and is again followed by elimination of NH_3 and reformation of the conjugated amidinium group. Imn^+ is expected as the favoured final product of this reaction as (a) its formation is entropically favourable due to the loss of two equivalents of gaseous NH_3, (b) reformation of the conjugated amidinium system is thermodynamically favourable, and (c) intramolecular ring-closure is kinetically preferred to intermolecular reaction with further FA^+*

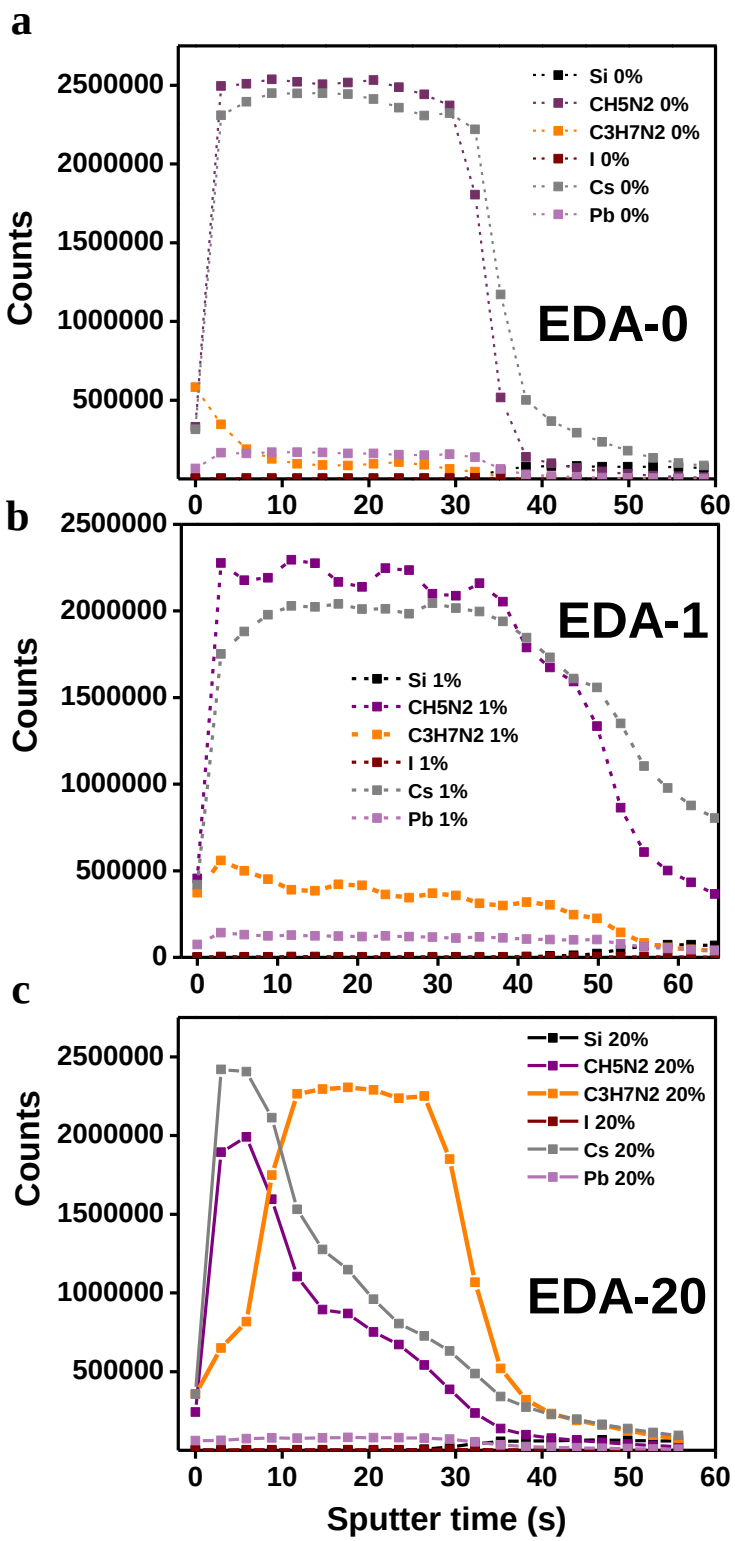

Figure S31*: (a) ToF-SIMS depth profiling of EDA-0 (dotted lines) (b) EDA-1 (dashed lines) and (c) EDA-20 (solid lines). Peaks corresponding to Si (black), FA-CH5N2 (purple), 2-imidazolinium-C3H7N2 (orange), iodide (dark red), cesium (grey), lead (violet) are displayed for the three samples as a function of sputter time.*

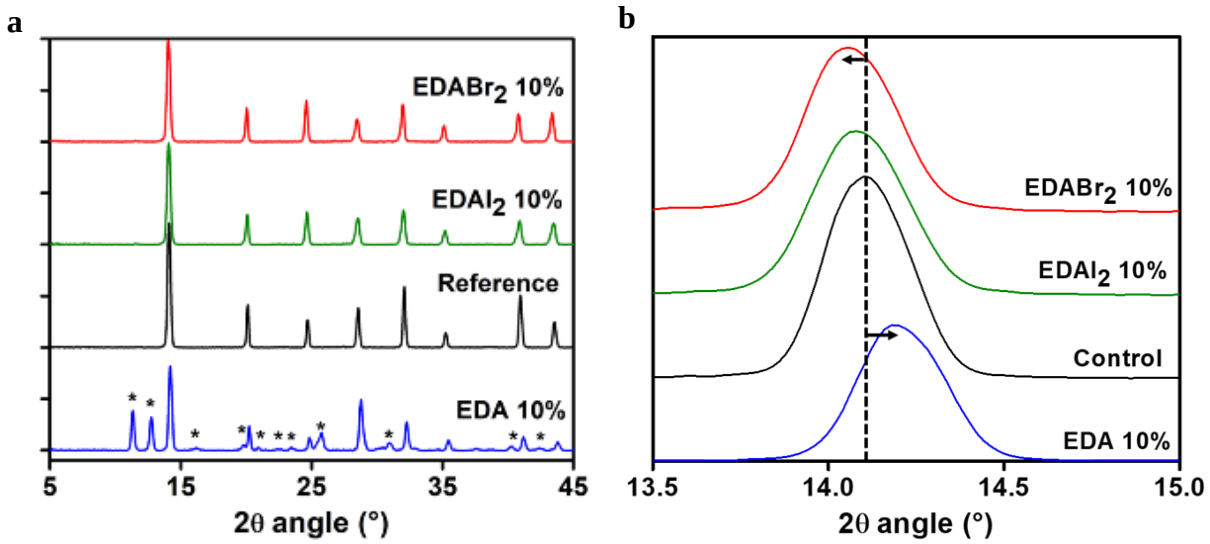

Figure S32: *(a) XRD patterns of the reference film (black), after addition of 10 mol% of $EDAH_2Br_2$ (red), $EDAH_2I_2$ (green) and EDA (blue). Peaks denoted with * correspond to the 4H polytype phase. (b) Highlight on the region from 13.5° to 15° of the patterns shown in (a). The dashed line follows the signal of the (100) plane of the cubic phase of the control and the arrows indicates the shift to smaller angles in the case of $EDAH_2I_2$ and $EDAH_2Br_2$ addition and larger angles with EDA.*

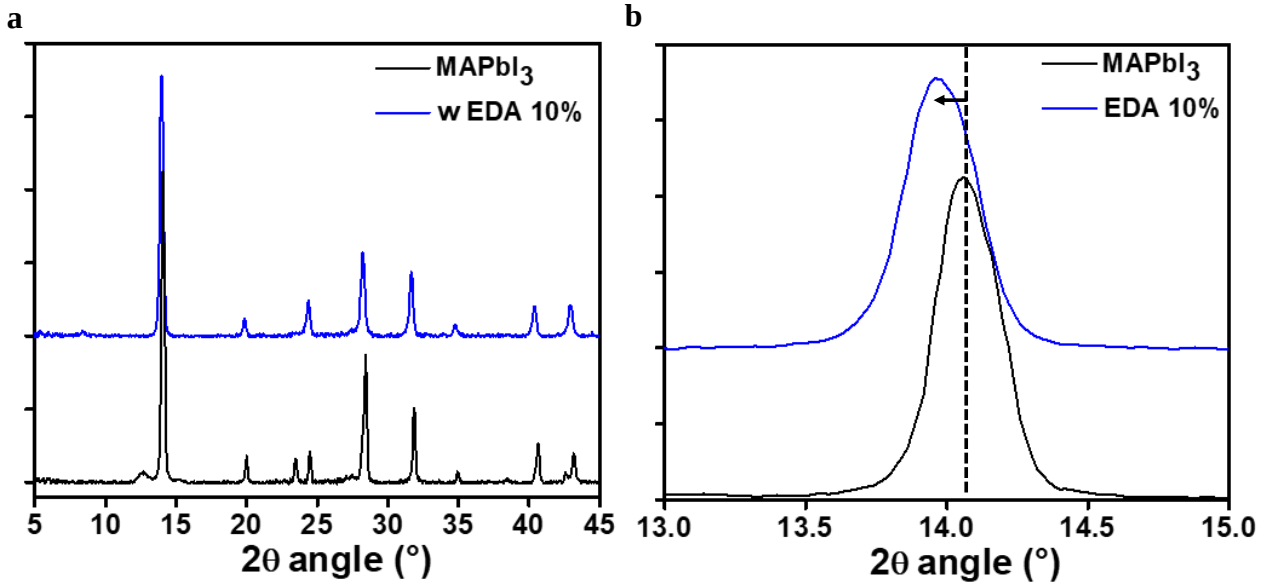

Figure S33: *(a) XRD pattern of MAPbI3(black) and with the addition of 10 mol% EDA (blue). (b) Zoom on the (100) peak of the alpha phase. The arrows show the shift to lower angles with 10% EDA*

References

(1) Jariwala, S.; Sun, H.; Adhyaksa, G. W. P.; Lof, A.; Muscarella, L. A.; Ehrler, B.; Garnett, E. C.; Ginger, D. S. Local Crystal Misorientation Influences Non-Radiative Recombination in Halide Perovskites. *Joule* **2019**, *3* (12), 3048–3060.

(2) deQuilettes, D. W.; Koch, S.; Burke, S.; Paranji, R. K.; Shropshire, A. J.; Ziffer, M. E.; Ginger, D. S. Photoluminescence Lifetimes Exceeding 8 Ms and Quantum Yields Exceeding 30% in Hybrid Perovskite Thin Films by Ligand Passivation. *ACS Energy Lett.* **2016**, *1* (2), 438–444.

(3) Momma, K.; Izumi, F. VESTA 3 for Three-Dimensional Visualization of Crystal, Volumetric and Morphology Data. *J. Appl. Crystallogr.* **2011**, *44* (6), 1272–1276.

(4) Al-Ashouri, A.; Köhnen, E.; Li, B.; Magomedov, A.; Hempel, H.; Caprioglio, P.; Márquez, J. A.; Morales Vilches, A. B.; Kasparavicius, E.; Smith, J. A.; Phung, N.; Menzel, D.; Grischek, M.; Kegelmann, L.; Skroblin, D.; Gollwitzer, C.; Malinauskas, T.; Jošt, M.; Matič, G.; Rech, B.; Schlatmann, R.; Topič, M.; Korte, L.; Abate, A.; Stannowski, B.; Neher, D.; Stolterfoht, M.; Unold, T.; Getautis, V.; Albrecht, S. Monolithic Perovskite/Silicon Tandem Solar Cell with >29% Efficiency by Enhanced Hole Extraction. *Science* **2020**, *370* (6522), 1300–1309.

(5) Kieffer, J.; Karkoulis, D. PyFAI, a Versatile Library for Azimuthal Regrouping. *J. Phys. Conf. Ser.* **2013**, *425* (20), 202012.

(6) Gratia, P.; Zimmermann, I.; Schouwink, P.; Yum, J.-H.; Audinot, J.-N.; Sivula, K.; Wirtz, T.; Nazeeruddin, M. K. The Many Faces of Mixed Ion Perovskites: Unraveling and Understanding the Crystallization Process. *ACS Energy Lett.* **2017**, *2* (12), 2686–2693.

(7) Zhang, Z.; Zhu, Y.; Wang, W.; Zheng, W.; Lin, R.; Huang, F. Growth, Characterization and Optoelectronic Applications of Pure-Phase Large-Area $CsPb_2Br_5$ Flake Single Crystals. *J. Mater. Chem. C* **2018**, *6* (3), 446–451.

(8) Hu, Y.; Aygüler, M. F.; Petrus, M. L.; Bein, T.; Docampo, P. Impact of Rubidium and Cesium Cations on the Moisture Stability of Multiple-Cation Mixed-Halide Perovskites. *ACS Energy Lett.* **2017**, *2* (10), 2212–2218.

(9) Glushkova, A.; Arakcheeva, A.; Pattison, P.; Kollár, M.; Andričević, P.; Náfrádi, B.; Forró, L.; Horváth, E. Influence of the Organic Cation Disorder on Photoconductivity in Ethylenediammonium Lead Iodide, $NH_3CH_2CH_2NH_3PbI_4$. *CrystEngComm* **2018**, *20* (25), 3543–3549.

(10) Spanopoulos, I.; Ke, W.; Stoumpos, C. C.; Schueller, E. C.; Kontsevoi, O. Y.; Seshadri, R.; Kanatzidis, M. G. Unraveling the Chemical Nature of the 3D "Hollow" Hybrid Halide Perovskites. *J. Am. Chem. Soc.* **2018**, *140* (17), 5728–5742.

(11) Haris, M. P. U.; Bakthavatsalam, R.; Shaikh, S.; Kore, B. P.; Moghe, D.; Gonnade, R. G.; Sarma, D. D.; Kabra, D.; Kundu, J. Synthetic Control on Structure/Dimensionality and Photophysical Properties of Low Dimensional Organic Lead Bromide Perovskite. *Inorg. Chem.* **2018**, *57* (21), 13443–13452.